ACS OMEGA

http://pubs.acs.org/journal/acsodf

Article

Recyclable Target Metal-Enhanced Fluorometric Naked Eye Aptasensor for the Detection of Pb^{2+} and Ag^{+} Ions Based on the Structural Change of $CaSnO_3$@PDANS-Constrained GC-Rich ssDNA

Arunjegan Amalraj, Rajaji Pavadai, and Panneerselvam Perumal*

Cite This: *ACS Omega* 2021, 6, 30580−30597

Read Online

ACCESS | Metrics & More | Article Recommendations | Supporting Information

ABSTRACT: Reliable, label-free, and ultraselective detection of Pb^{2+} and Ag^{+} ions is of paramount importance for toxicology assessment, human health, and environmental protection. Herein, we present a novel recyclable fluorometric aptasensor based on the Pb^{2+} and Ag^{+}-induced structural change of the GC-rich ssDNA (guanine cytosine-rich single-strand DNA) and the differences in the fluorescence emission of acridine orange (AO) from random coil to highly stable G-quadruplex for the detection of Pb^{2+} and Ag^{+} ions. More interestingly, the construction and principle of the aptasensor explore that the GC-rich ssDNA and AO can be strongly adsorbed on the $CaSnO_3$@PDANS surface through the $\pi-\pi$ stacking, hydrogen-bonding, and metal coordination interactions, which exhibit high fluorescence quenching and robust holding of the GC-rich ssDNA. However, in the presence of Pb^{2+}, the specific G-rich ssDNA segment could form a stable G-quadruplex via G4−Pb^{2+} coordination and capture of AO from the $CaSnO_3$@PDANS surface resulting in fluorescence recovery (70% enhancement). The subsequent addition of Ag^{+} ion induces coupled cytosine base pairs in another segment of ssDNA to get folded into a duplex structure together with the G-quadruplex, which highly stabilizes the G-quadruplex resulting in the maximum recovery of AO emission (99% enhancement). When the Cys@Fe_3O_4Nps are added to the above solution, the sensing probe was restored by complexation between the Cys in the Cys@Fe_3O_4Nps and target metal ions, resulting in the fabrication of a highly sensitive recyclable Pb^{2+} and Ag^{+} assay with detection limits of 0.4 and 0.1 nM, respectively. Remarkably, the Cys@Fe_3O_4Nps can also be reused after washing with EDTA. The utility of the proposed approach has great potential for detecting the Pb^{2+} and Ag^{+} ions in environmental samples with interfering contaminants.

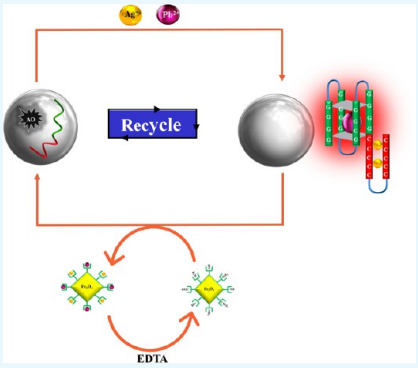

1. INTRODUCTION

Heavy metals are tightly regulated in biological structures and play critical roles in various physiological processes. The toxic metal-ion homeostasis disruptions are related to a host of serious illnesses, including cancer and AIDS. Thus, the heavy-metal ions are very hazardous and life-threatening for humans, animals, and marine life, and the most harmful metals are Pb^{2+}, Ag^{+}, Hg^{2+}, Cd^{2+}, As^{3+}, Al^{3+}, etc.[1,2] These metal compounds do not decompose in water, and they combine with other pollutants to produce more toxic compounds that could cause serious damage to the ecology and organisms. Though some elements in trace amounts are essential to life (e.g., Fe, Ag, and Al), they become toxic if their presence is in excess. Especially, lead and silver ions (Pb^{2+} and Ag^{+}) are known for their toxic, nondegradable, and carcinogenic nature as they are frequently released into the environment through industrial sewages.[3,4]

Lead and silver ions are widely found in electric storage batteries, paint pigments, pipes, photography, pharmacy, and jewelry, and their coexistence results in the contamination of air, water, food, and soil, which have the capacity to damage the entire biological system. Even low concentrations of Pb^{2+} and Ag^{+} ions in the blood can damage the cardiovascular, neurological, reproductive, and developmental systems of the human body and may lead to convulsions and death.[5,6] For example, Pb^{2+} or Ag^{+} ions can bind to several negatively charged groups, such as sulfhydryl in enzymes and proteins in the body, which affect many metabolic pathways in the cell, such as energy production, protein, and nucleic acid synthesis, thus affecting the cell functionality and development. Moreover, the Pb^{2+} and Ag^{+} ions adsorbed by the human body replace certain essential metal elements like Ca^{2+}, Mg^{2+}, and Zn^{2+}, which leads to acute damage in the bones.[7−9] Therefore, it is of paramount importance to develop a rapid, highly accurate, and relatively cost-effective method for the detection of Pb^{2+} and Ag^{+} in real samples.

Received: August 11, 2021
Accepted: September 29, 2021
Published: November 3, 2021

https://doi.org/10.1021/acsomega.1c04319
ACS Omega 2021, 6, 30580−30597

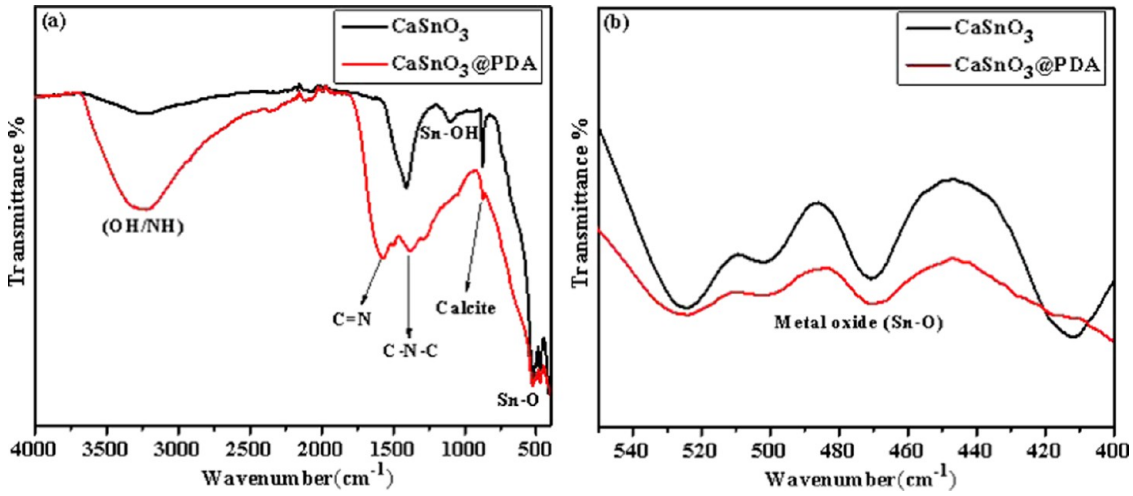

Figure 1. (a) FT-IR spectra of $CaSnO_3$ and $CaSnO_3$@PDANS and (b) high-resolution FT-IR spectra of the M−O bond.

So far, numerous analytical techniques have been established in the detection of Pb^{2+} and Ag^+ ions, such as high-pressure liquid chromatography (HPLC), atomic absorption spectroscopy (AAS), inductively coupled plasma atomic emission spectroscopy (ICP-OES), flame atomic absorption spectroscopy (FAAS), and cloud point extraction method, etc.[10−16] These extensively used instrumental analytical methods have significant drawbacks, such as involvement of costly equipment, difficulty in sample preparation, need for a well-trained analyst, etc. Moreover, currently, fluorescence, electrochemiluminescence, photoluminescence, colorimetric, and SPR methods were used, but these common optical methods also have some limitations, including time consumption, low compatibility, frequent electrode fouling, low reproducibility, selectivity, and stability. In response to these limitations, the past decades have seen great progress in the development of heavy-metal sensors based on guanine−lead [G4−Pb^{2+}] and cytosine−silver [C−Ag^+−C] coordination chemistry using colorimetric, fluorescence, and electrochemical detection techniques,[3,6,17−19] among which the fluorescence technique is the most convenient, economically feasible, and companionable for the sensitive and specific detection of Pb^{2+} and Ag^+ ions.

Recently, increased attention is focused on the label or label-free DNA-based fluorescence biosensor using various nanomaterials[20,21] for the detection of targets because of their unique chemical or physical properties.[17,22,23] Currently, three kinds of approaches involving the nanomaterial-based DNA fluorescence method are established for the detection of toxic metal exposure: The first approach involves the usage of DNA as a specific binding ligand for metal sensing due to extreme specific coordination interaction between the metal (Pb^{2+} and Ag^+) and DNA base pairs. Guschlbauer et al. reported that Pb^{2+} could interact with the guanine (G) base to form a stable G-quadruplex structure via G4−Pb^{2+} from the random coil DNA structure. Ono et al. reported that Ag^+ could influence the conformational switch of a cytosine (C)-rich DNA from a random coil to the duplex DNA through the C−Ag^+−C coordinate bonds. Thus, the specific G4−Pb^{2+} and C−Ag^+−C interaction ensures excellent selectivity for the Pb^{2+} and Ag^+ detections instead of other metal ions. The second approach involves the usage of fluorophore, an important fluorescent signal probe for all of the DNA-based fluorescence biosensors. The third approach involves the usage of a nanomaterial as a DNA adsorbent and fluorescence quencher due to several interactions such as $\pi-\pi$ stacking, electrostatic, van der Waals, metal coordination, and hydrogen bonding, which enhances the sensitivity of the detection (sensing ability). Based on this phenomenon, a large variety of nanomaterials are established, including graphene oxide (GO), metal−organic framework (MOF), metal oxide, MoS_2 nanosheets, silver and gold nanoparticles, etc.[24−30] They are widely used in the fabrication of heavy-metal sensors because of their adsorption and fluorescence quenching capability, which promotes sensing performance.

Several research groups are now oriented on the development of interconnected nanomaterials between the organic polymers and metal oxide to completely investigate the composite material for a wide variety of applications in optical, photoelectric, and photocatalytic fields. Hence, the research outline in this paper focuses on the synthesis of a novel $CaSnO_3$@PDANS using a metal coordination mechanism, which exhibits high quenching and DNA adsorption ability. Metal coordination is the principal mechanism for fabricating materials, while its application in DNA adsorption and fluorescence quenching is rarely explored. Polydopamine (PDA) as an organic polymer is considered as the most common material due to its appropriate thermal stability, simple and cost-effective production methods, excellent biocompatibility, biodegradability, and surface coating properties compared to other polymers. The PDA has found widespread applications in drug administration, photothermal treatment, tissue engineering, cell adhesion, and biosensors.[31] PDA nanoparticles have the ability to adsorb DNA and quench fluorescence, which results in new analytical possibilities. The PDA is also a good metal ligand, which initiated the research line for being a good platform for creating coordination-based DNA-adsorbing and fluorescence quenching materials.[32] Hence, the current research is focused on the incorporation of the PDA with $CaSnO_3$ to synthesize the $CaSnO_3$@PDA nanosphere, which reveals better DNA adsorption and fluorescence quenching ability compared to pure PDA or $CaSnO_3$.

Herein, the polydopamine-terminated $CaSnO_3$ inorganic−organic composite nanosphere was prepared using a simple ultrasonication method, which is used to immobilize the GC-

https://doi.org/10.1021/acsomega.1c04319
ACS Omega 2021, 6, 30580−30597

rich ssDNA and decrease the AO intensity. Moreover, a suitable specific GC-rich ssDNA sequence possessing a higher affinity to form duplex along with G-quadruplex was developed. Hence, the research proposed a facile target metal enhancing the fluorescence strategy by integrating $\pi-\pi$ stacking and metal coordination interaction of $CaSnO_3$@PDANS with specific GC-rich ssDNA to develop a Pb^{2+} and Ag^{+} recyclable aptasensor. The superiority of this biosensor platform states that the Pb^{2+}- and Ag^{+}-ion detection probe was recycled using Cys@Fe_3O_4Nps, and it can be reused by treating with EDTA. Compared with the conventional Pb^{2+} and Ag^{+} aptasensor, this method provides acceptable recycling sensing results with excellent sensitivity and selectivity.

2. RESULTS AND DISCUSSION

2.1. Characterization. The morphology, crystallinity, and chemical bonding of $CaSnO_3$ and $CaSnO_3$@PDANS were characterized successively. FT-IR spectroscopy confirmed the existence of several functional groups and chemical bonding of PDA, which were successfully assigned on the surface of $CaSnO_3$, and the results are illustrated in Figure 1a. For a pure $CaSnO_3$ nanomaterial, the peak around 1103 cm^{-1} was attributed to the stretching vibration of the Sn−OH bond. The peaks below 700 cm^{-1} corresponded to the metal−oxygen bonding, as revealed in Figure 1b. Especially, Sn−O bonds were observed at 470 and 412 cm^{-1}, and a specific characteristic band was observed at 525 cm^{-1}, which is the stretching vibration of the O−Sn−O bonding. Moreover, the calcite possessed a less intense peak at 873 cm^{-1}, which may be attributed to the presence of calcium and oxygen in the as-synthesized $CaSnO_3$. For PDA, two clear characteristic absorption bands around 1388 and 1567 cm^{-1} are due to the C−N−C and C═N stretching vibration modes, respectively. Comparatively, $CaSnO_3$@PDANS displays the characteristic absorption bands of both $CaSnO_3$ and PDA, which evidently implied the successful incorporation of the PDA on the surface of $CaSnO_3$.[33,34]

Furthermore, the XRD measurements of $CaSnO_3$ and $CaSnO_3$@PDANS are shown in Figure 2. The obtained diffraction patterns of $CaSnO_3$ reveal the presence of several peaks at 2θ = 18.8, 21.8, 30.9, 33.3, 37.0, 38.3, 47.8, 50.6, 57.4, 62.4, 69.8, 73.8, and 77.9, which can be attributed to the (101), (110), (020), (112), (021), (121), (022), (221), (213), (312), (133), (233), and (234) planes, respectively. They clearly indicate the formation of a standard single perovskite phase with an orthorhombic crystal structure (JCPDS 01-077-1797).[35] The spectral patterns show sharp peaks, indicating the crystalline nature of $CaSnO_3$. Moreover, the XRD pattern of $CaSnO_3$@PDANS reveals the absence of noticeable peaks. However, the intensity of $CaSnO_3$@PDANS peaks is low rather than that of $CaSnO_3$ peaks, which suggests that the PDA nanofibers were successfully grown on the surface of the orthorhombic $CaSnO_3$, resulting in consequential changes in morphology as nanosphere.

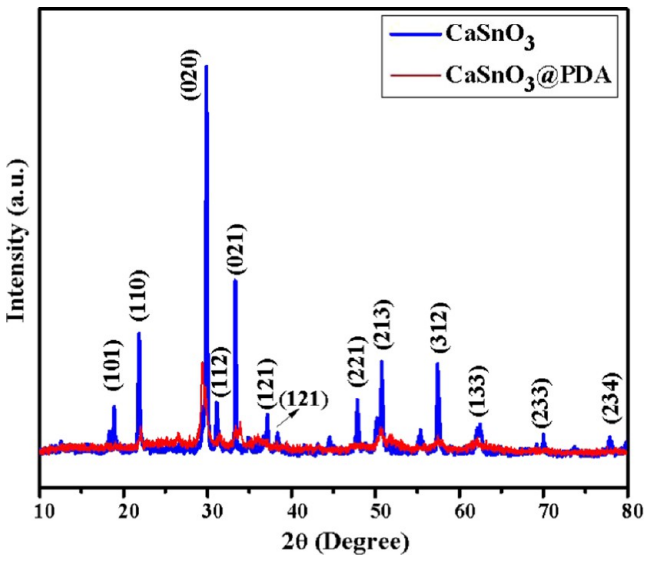

Figure 2. XRD patterns of $CaSnO_3$ and $CaSnO_3$@PDANS.

The HRSEM analysis was done for pure $CaSnO_3$ and $CaSnO_3$@PDANS for further exploration of morphological features, as revealed in Figure 3. Figure 3a,b depicts the typical HRSEM images of $CaSnO_3$ nanoparticles, which exemplify the flowerlike architecture with hierarchical structures. The HRSEM images of $CaSnO_3$@PDANS (Figure 3c,d) show that the nanospheres were formed with the successful incorporation of PDA on the surface of the $CaSnO_3$ microflower, which is further verified using the HRTEM observations (Figure 4). The HRTEM image of the $CaSnO_3$@PDANS exhibits a smooth and homogeneous sphere structure. Moreover, a higher-magnification (5 nm) HRTEM image was taken to identify its internal nanostructure. The different colors represent the core/shell nature of the nanosphere, with the PDA being the outermost off-white layer and the inner black core represents $CaSnO_3$, as shown in Figure 4c,d. This result proves that the nanosphere with $CaSnO_3$ as the core and a PDA layer as the outer shell were successfully synthesized. From the energy-dispersive X-ray spectrum of $CaSnO_3$ and $CaSnO_3$@PDANS (Figure 5a,b), the calcium, tin, oxygen, and carbon elements are obviously observed, suggesting that the two-layer nanostructure $CaSnO_3$@PDANS was effectively fabricated.

XPS was employed to investigate the surface composition and the oxidation states of the elements of $CaSnO_3$@PDANS shown in Figure 6. The full-range XPS analysis of $CaSnO_3$@PDANS revealed in Figure 6a clearly showed five characteristic peaks of Sn 3d, Ca 2p, C 1s, N 1s, and O 1s, corresponding to the binding energies of 485.4, 346.4, 284.4, 399.7, and 532.6 eV. The 3d Sn spectra of $CaSnO_3$@PDANS shown in Figure 6b can be deconvoluted into two subpeaks with binding energies of 486.7 and 495.1 eV that can be assigned to Sn $3d_{3/2}$ and Sn $3d_{5/2}$, respectively, confirming Sn in the +4 oxidation state. Figure 6c depicts high-resolution spectra of the Ca 2p distinct peaks at 346.8 and 350.4 eV,[36] indicating the formation of Ca $2p_{1/2}$ and Ca $2p_{3/2}$ associated with the oxidation state Ca^{2+}. Further, the high-resolution C 1s spectra were fitted with two peaks at about 284.5 and 286.2 eV, which could be attributed to sp^2 (C═C) and sp^3 (C−C) carbon, respectively (Figure 6d). The N 1s spectra possessed a single peak at 398.0 eV, ascribing the presence of C−N in $CaSnO_3$@PDANS (Figure 6e). Additionally, the broad and asymmetric peaks for O 1s at 531.2 and 532.3 eV indicate the presence of two types of oxygen termed adsorbed oxygen and lattice oxygen,[37] respectively, as shown in Figure 6f. Moreover, the functionality of the $CaSnO_3$@PDANS determined using the XPS was compatible with the corresponding FT-IR spectra.

2.2. Effect of DNA Sequence on Fluorescence Enhancement. The fluorescence-enhancing ability strongly

https://doi.org/10.1021/acsomega.1c04319
ACS Omega 2021, 6, 30580−30597

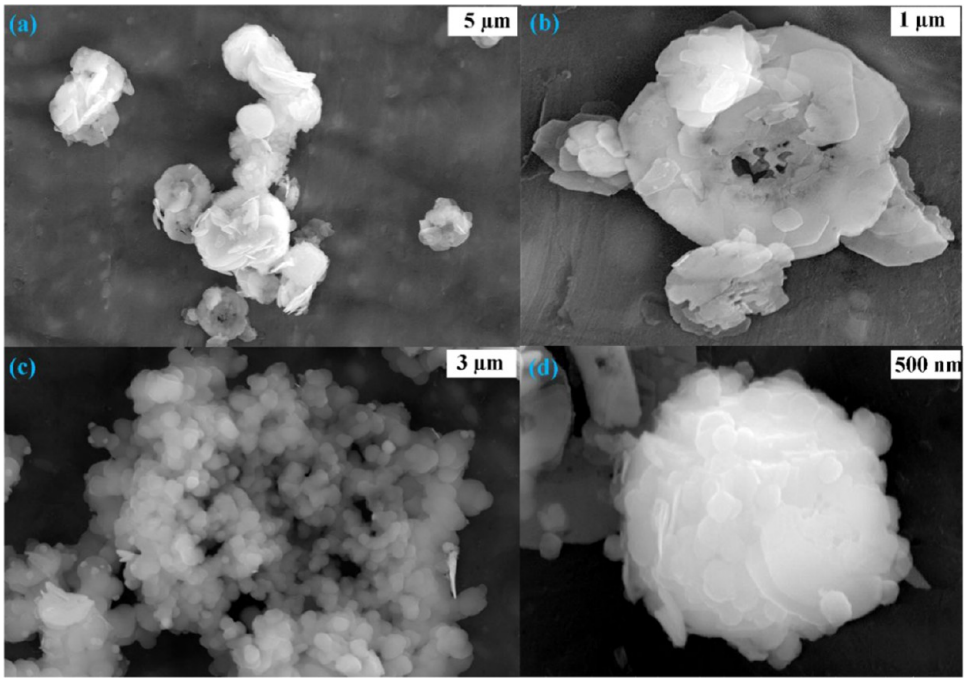

Figure 3. HRSEM images of $CaSnO_3$ (a, b) and $CaSnO_3$@PDANS (c, d).

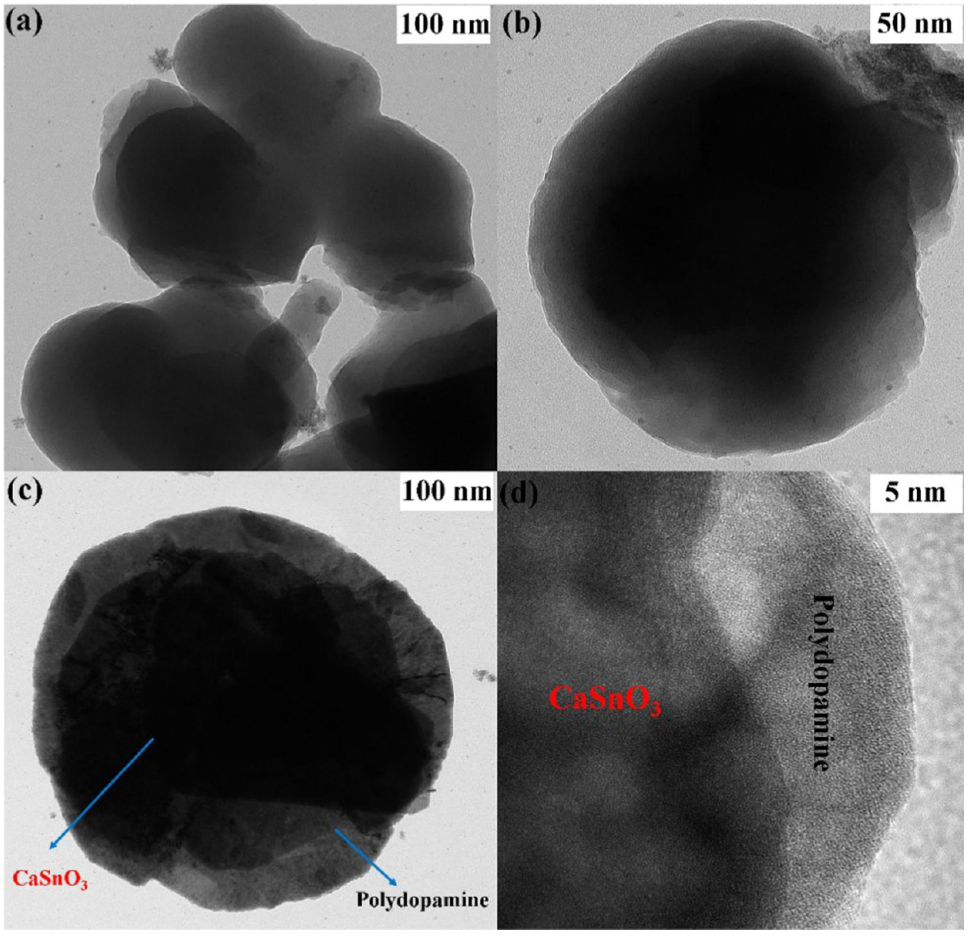

Figure 4. HRTEM images of $CaSnO_3$@PDANS (a–d).

depends on the nature of the GC-rich ssDNA base pair sequence. This is because only a stable DNA G-quadruplex structure can strongly capture the AO from the surface of $CaSnO_3$@PDANS, which resulted in the enhancement of fluorescence intensity. Accordingly, the fluorescence-enhancing ability was analyzed using five different kinds of ssDNA to

https://doi.org/10.1021/acsomega.1c04319
ACS Omega 2021, 6, 30580−30597

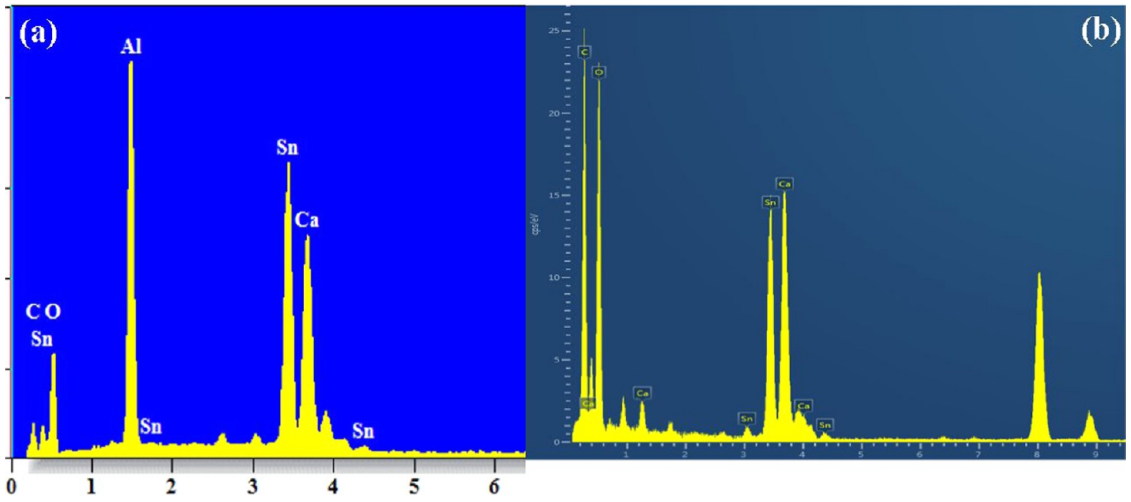

Figure 5. EDX spectra of $CaSnO_3$ (a) and $CaSnO_3$@PDANS (b).

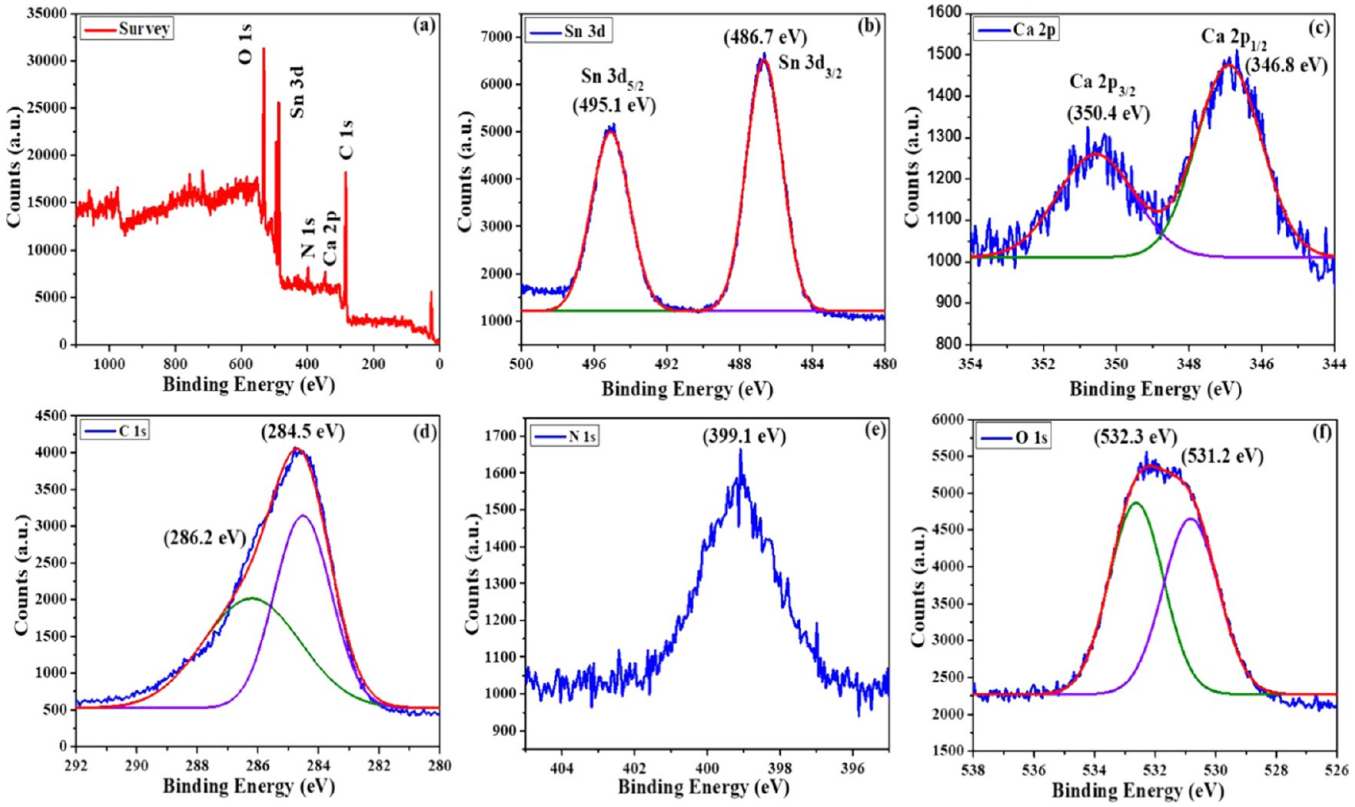

Figure 6. (a) XPS spectra of the obtained $CaSnO_3$@PDANS. (b–f) High-resolution XPS spectra of Sn 3d, Ca 2p, C 1s, N 1s, and O 1s of $CaSnO_3$@PDANS, respectively.

determine the suitable variant for improving the sensing performance. To estimate the influence of DNA sequence on fluorescence enhancement, DNA1, DNA2, DNA3, DNA4, DNA5 (each 500 nM), and 500 nM AO were separately incubated with $CaSnO_3$@PDANS in a Tris-HCl buffer. The appropriate concentration of Pb^{2+} and Ag^{+} was applied to induce fluorescence recovery. Finally, the fluorescence enhancement was plotted as a function of DNA sequence, as shown in Figure 7.

In this research, the transformation of DNA structure involved specially designed DNA, which is rich in guanine and cytosine with specific loops. The transition of DNA structure would form a duplex along with G-quadruplex conformation induced by Pb^{2+} and Ag^{+} ions. The fluorescence intensity histogram clearly illustrates that DNA3 possesses higher fluorescence, which indicates the formation of a highly stable G-quadruplex due to the selective DNA sequence, length, orientation, and nature of the loops.

DNA3: 3′-TAGGGTTGGGTATGGGAAGGGTCCCTC-CAACCTATACCTTCCACCCA-5′

The interesting and best-sensing response by DNA3 is due to four specific guanine tracks, each having three guanine bases. The addition of Pb^{2+} ions results in the combination of four guanine bases obtained from four guanine tracks. They

https://doi.org/10.1021/acsomega.1c04319
ACS Omega 2021, 6, 30580−30597

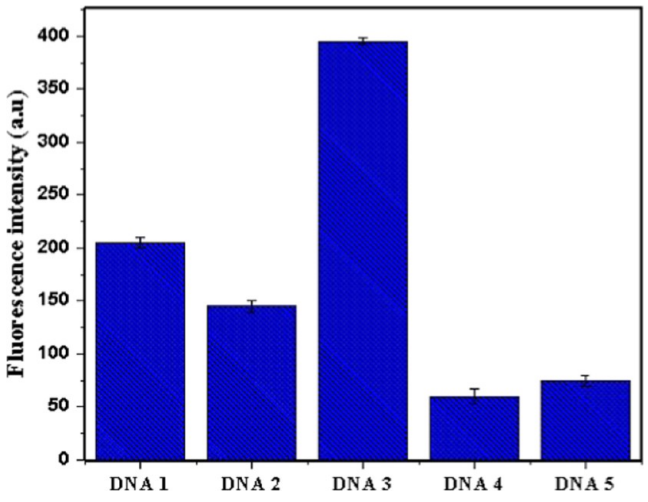

Figure 7. Fluorescence emission vs various DNA.

form a square planar structure, which is termed a guanine tetrad realized through Hoogsteen hydrogen bonding. Then, the four guanine tetrads stack on each other to form a G-quadruplex. Further, the duplex formation along with G-quadruplex occurs after the addition of Ag^{+} because of the long cytosine-rich second segment of DNA3, which highly stabilizes the G-quadruplex structure. Especially, DNA3 also has a short loop length compared to others, which could help in the formation of a highly stable G-quadruplex (Figure 8). Thus, we conclude that DNA3 possesses strong ability to form a duplex structure along with G-quadruplex using specific G- and C-rich segments with appropriate loops. As a result, it is selected for the highly sensitive and selective detection of target metal ions.

2.3. Effect of CaSnO3@PDANS on the Sensor Ability. The AO/GC-rich ssDNA probe along with the target metal ion is used as a sensing platform for evaluating the AO fluorescence quenching ability and the DNA discrimination ability between the ssDNA and G-quadruplex using $CaSnO_3$@PDANS. Figure 9a reveals the fluorescence emission spectra of AO/GC-rich ssDNA and $CaSnO_3$@PDANS under different conditions with a maximum excitation wavelength of 490 nm. In $CaSnO_3$@PDANS, no emission peak was observed (curve A), inferring that $CaSnO_3$@PDANS did not cause interference tangibly with fluorescence experiments. Meanwhile, the AO/GC-rich ssDNA probe reveals intense fluorescence emission (curve B). However, in the presence of $CaSnO_3$@PDANS, the fluorescence emission was quenched to about 98% (curve C). This is because $CaSnO_3$@PDANS possesses strong ability to adsorb both AO- and GC-rich ssDNA through $\pi-\pi$ stacking (between nucleobases and aromatic rings of PDA), hydrogen-bonding (between $-NH_2$ and $-C{=}O$ groups of DNA and $-NH_2$ and $-OH$ groups of PDA), and metal coordination interactions. When target metal ions were added to the above solution, about 99% fluorescence was recovered due to the formation of a highly stable G-quadruplex (curve D). These changes illustrate that $CaSnO_3$@PDANS was not able to adsorb the G-quadruplex DNA due to the weak affinity of the G-quadruplex to the $CaSnO_3$@PDANS surface. Therefore, the above results indicate that $CaSnO_3$@PDANS possesses excellent fluorescence quenching ability and discrimination capability between the GC-rich ssDNA and the G-quadruplex.

Furthermore, a comparison was made between $CaSnO_3$@PDANS and graphene oxide, MoS_2 nanosheet, PDANps, and $CaSnO_3$, and the fluorescence quenching performance is revealed in Figure 9b. The AO/GC-rich ssDNA was mixed with the same concentration of $CaSnO_3$@PDANS, graphene oxide, MoS_2 nanosheet, PDANps, and $CaSnO_3$. It was found that $CaSnO_3$@PDANS showed the highest quenching performance and low signal background fluorescence due to the FRET process between the emission spectrum for the energy donor AO and the absorption spectrum for the energy acceptor $CaSnO_3$@PDANS.

On the other hand, Ca^{2+} and Sn^{4+} also contribute to the intrinsic DNA adsorption and the fluorescence quenching process due to the binding of the phosphate skeleton in DNA to the calcium and tin cations in $CaSnO_3$@PDANS. According

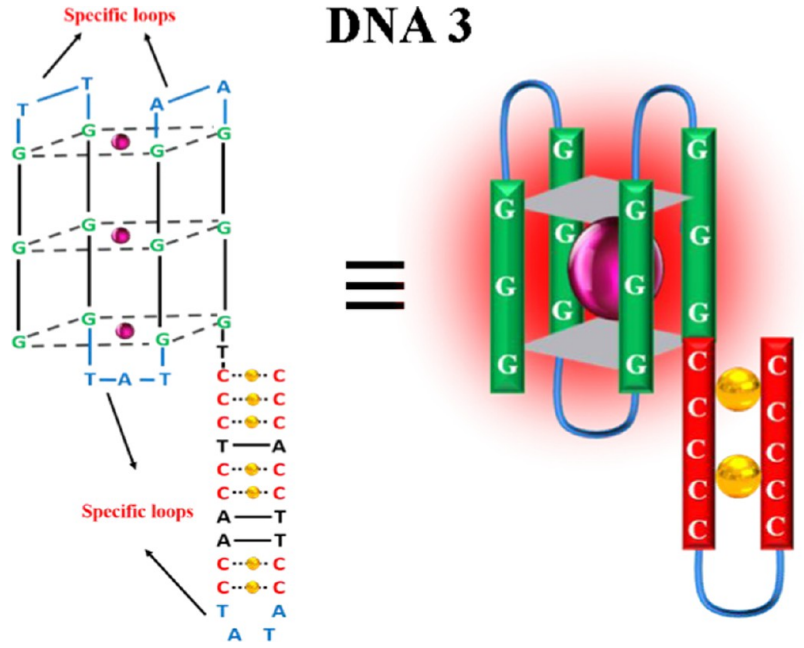

Figure 8. Graphical representation of DNA3.

https://doi.org/10.1021/acsomega.1c04319
ACS Omega 2021, 6, 30580−30597

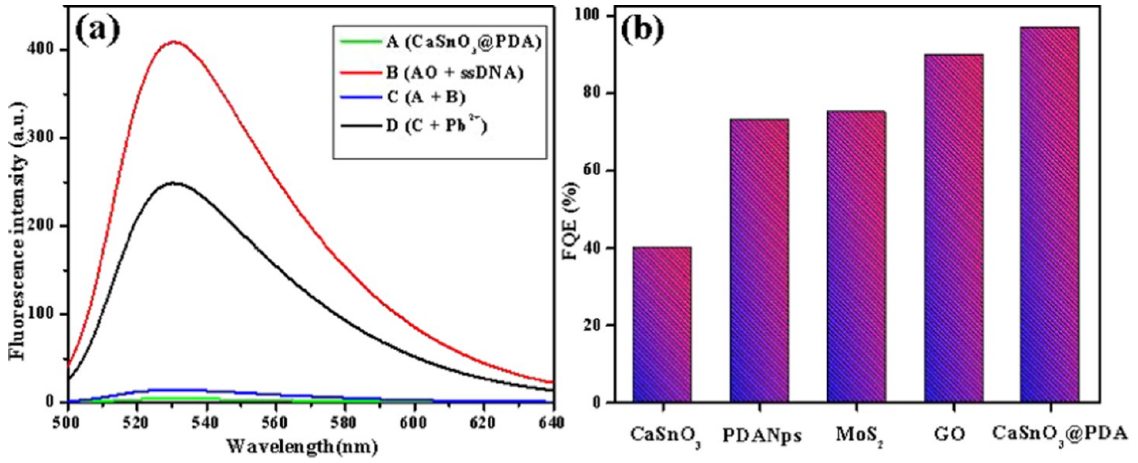

Figure 9. (a) Effect of $CaSnO_3$@PDANS on fluorescence response. (b) Comparison of fluorescence quenching efficiency (FQE %) with various nanomaterials.

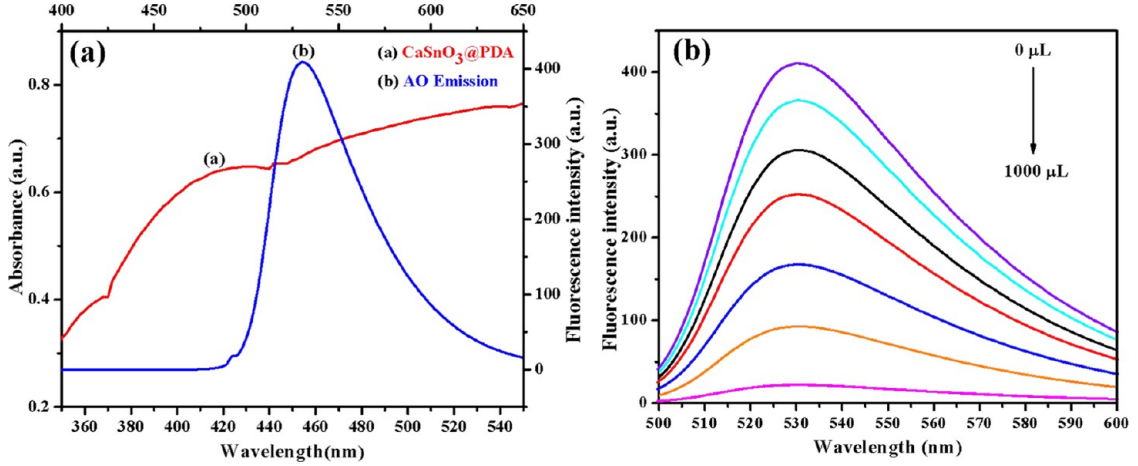

Figure 10. (a) $CaSnO_3$@PDANS UV–vis absorption spectra (curve a) and AO emission spectra (curve b). (b) Fluorescence spectra of AO emission in the presence of various quantities of $CaSnO_3$@PDANS.

to the hard–soft–acid–base concept, Ca^{2+}, being a hard Lewis acid, has a tendency to bind very firmly to phosphate (a hard Lewis base), which exhibits high quenching and adsorbing performance. At the same time, graphene oxide, MoS_2, PDANps, and metal oxides reveal low quenching performance compared to $CaSnO_3$@PDANS. The fluorescence quenching efficiency was estimated by the formula QE = $(F_P - F_M/F_P) \times 100\%$, where F_P represents the fluorescence emission of pure AO and F_M represents the fluorescence emission following the addition of $CaSnO_3$@PDANS to AO. According to the results, the fluorescence quenching efficiency of $CaSnO_3$@PDANS reached up to 98%. Hence, it is established that $CaSnO_3$@PDANS can be applied as an excellent fluorescence quencher and DNA adsorbent for the fluorescent biosensor.

2.4 FRET between AO and CaSnO3@PDACNS. From Figure 10a, the emission spectra of the AO largely overlap the absorption spectra of $CaSnO_3$@PDANS. Hence, $CaSnO_3$@PDANS effectively quenches the fluorescence of AO due to the FRET. According to the FRET process, the AO acts as an energy donor in this system, while $CaSnO_3$@PDANS acts as an energy acceptor (quencher).

To further confirm the FRET, the emission spectra of AO were examined in the $CaSnO_3$@PDANS-AO system at various amounts of $CaSnO_3$@PDANS. When the concentration of the donor AO was held constant at 50 μL (500 nM), the fluorescence intensities of the AO steadily decreased with increasing amount of $CaSnO_3$@PDANS from 0 to 1000 μL as revealed in Figure 10b. This implied that when more $CaSnO_3$@PDANS (acceptor) was introduced, more energy was transferred from AO to $CaSnO_3$@PDANS, which resulted in the quenching of fluorescence intensity.

2.5. Proposed Sensing Mechanism of the Pb^{2+} and Ag^+ Aptasensor. The detailed principle of the proposed targets enhanced fluorometric aptasensor strategy for Pb^{2+} and Ag^+ detection is presented in Schemes 1 and 2. Generally, this anticipated aptasensor was based on the structural change of DNA and the difference in the fluorescence intensity of AO from a GC-rich ssDNA to a highly stable G-quadruplex. This is because the stable G-quadruplex DNA can significantly enhance the AO fluorescence, whereas ssDNA or dsDNA does not. Initially, the fluorometric aptasensor probe was fabricated by the adsorption of GC-rich ssDNA (specifically designed guanine-rich and cytosine-rich segment DNA) and AO onto the $CaSnO_3$@PDANS surface via $\pi-\pi$ stacking, hydrogen-bonding, and metal coordination interactions, resulting in low AO fluorescence signals owing to the FRET process as revealed in Figure 11a(b).

https://doi.org/10.1021/acsomega.1c04319
ACS Omega 2021, 6, 30580–30597

Scheme 1. Schematic Illustration of the Recyclable Fluorometric Detection of Pb^{2+} and Ag^{+} Using the $CaSnO_3$@PDANS/GC-Rich ssDNA/AO Detection Probe

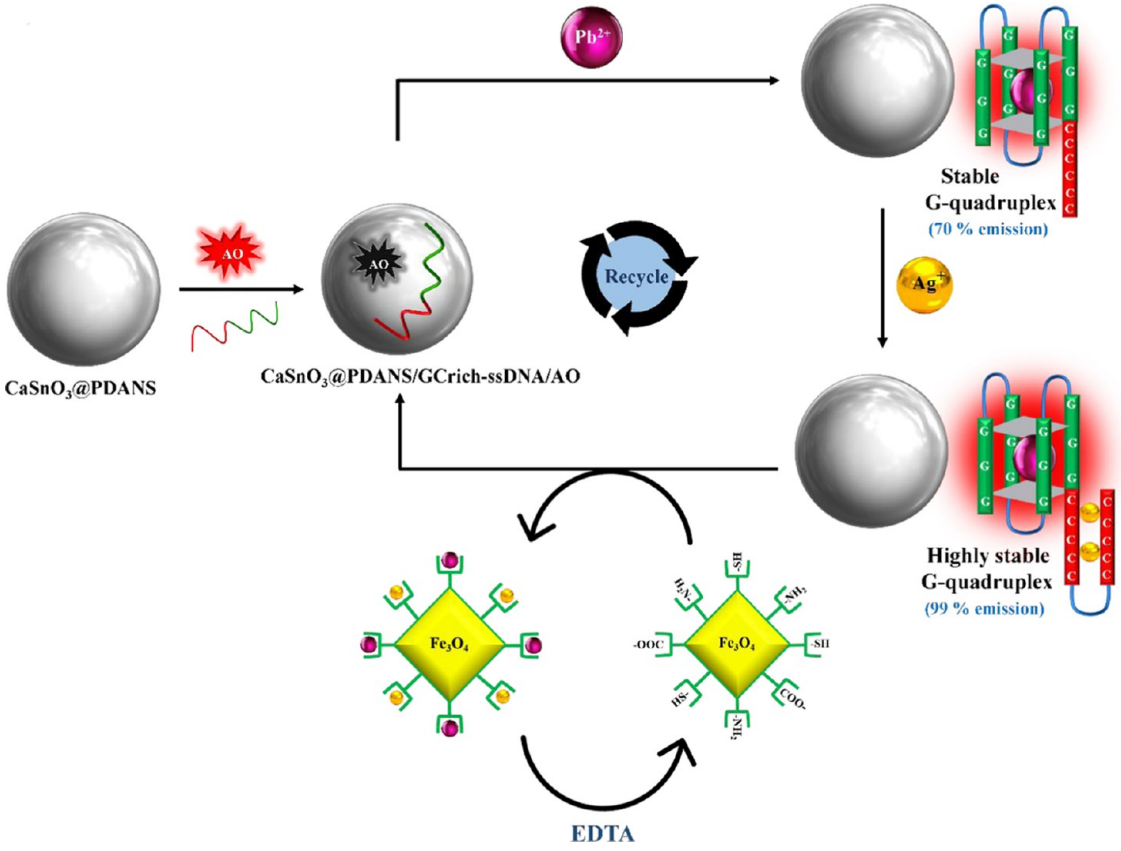

Scheme 2. Vivid Illustration of Regeneration of a Sensing Probe by the Addition of Cys@Fe_3O_4Nps

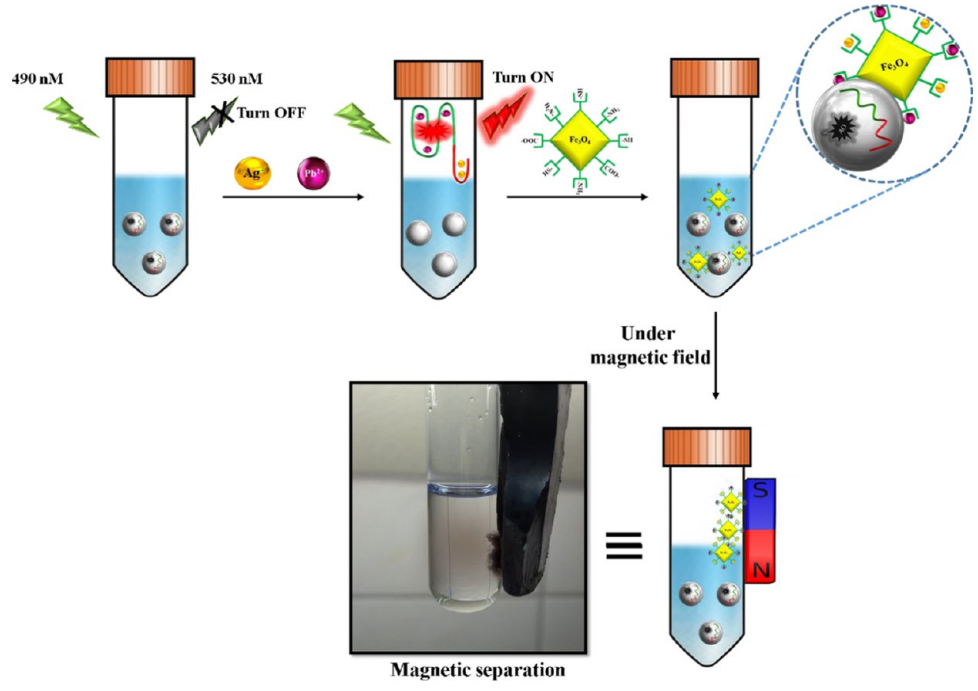

In the presence of Pb^{2+}, due to the special induction capability of Pb^{2+} to the G-rich segment of the GC-rich ssDNA, G-quadruplex is formed via G4−Pb^{2+} at the third terminal of the GC-rich ssDNA. The AO fluorescence emission gradually increased, attributing to the strong affinity between the AO and G-quadruplex DNA resulting in the removal of AO from $CaSnO_3$@PDANS. The fluorescence emission increase was about 70% at a maximal concentration

https://doi.org/10.1021/acsomega.1c04319
ACS Omega 2021, 6, 30580−30597

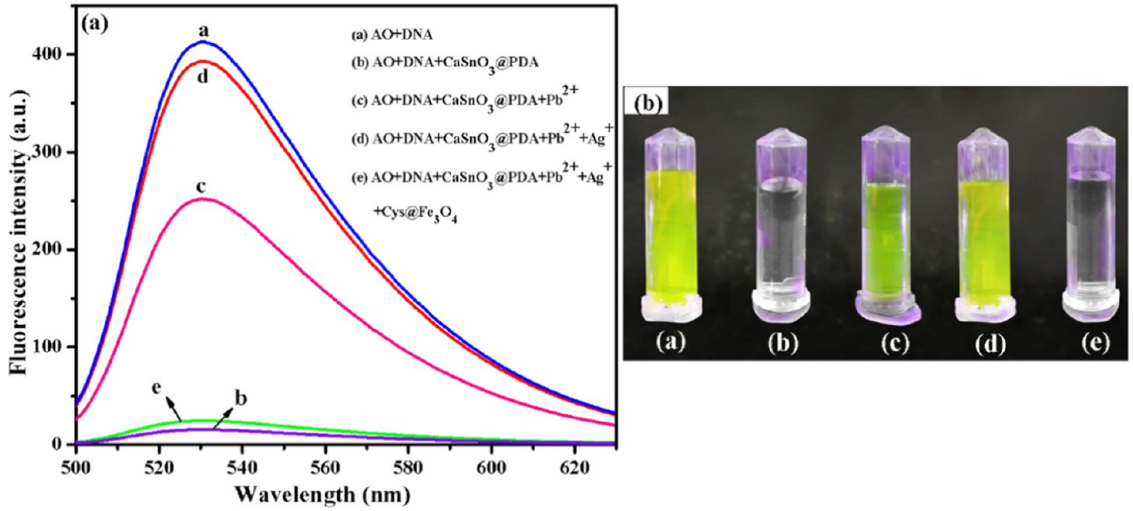

Figure 11. (a) Fluorescence spectra of AO emission during the different processes. (b) Fluorescence distinction of AO during different processes by the naked eye under UV light. ((a) AO + DNA, (b) AO + DNA + $CaSnO_3$@PDANS, (c) AO + DNA + $CaSnO_3$@PDANS + Pb^{2+}, (d) AO + DNA + $CaSnO_3$@PDANS + Pb^{2+} + Ag^+, and (e) AO + DNA + $CaSnO_3$@PDANS + Pb^{2+}+Ag^+ + Cys@Fe_3O_4Nps).

Scheme 3. Schematic Representation of the Reusability of Cys@Fe_3O_4Nps

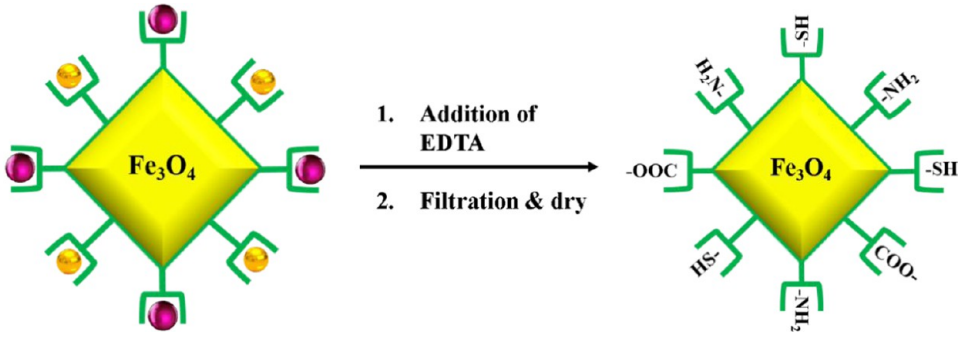

of Pb^{2+} Figure 11a(c). When the Pb^{2+} concentration was higher, the fluorescence emission remains almost unchanged. However, in the presence of Ag^+ ions, it induces the coupled cytosine residues in the C-rich segment, resulting in the folding of a duplex along with a G-quadruplex. This is attributed to the fact that the C−C base pair may specifically trap Ag^+ ion, resulting in the formation of the C−Ag^+−C complex. Furthermore, the formed duplex structure at the 5′-terminal of the G-quadruplex highly stabilizes the G-quadruplex, resulting in a high recovery (99%) of AO fluorescence, as revealed in Figure 11a(d). When the L-cysteine-decorated magnetic nanoparticle (Cys@Fe_3O_4Nps) was added to the above solution, it strongly attracts the Ag^+ and Pb^{2+} ions due to the complex capabilities of the multiple −SH, $-NH_2$, and −COOH groups in the Cys. The metal ions and electrostatic adsorption also played a significant role in metal adsorption. This results in the regeneration of the starting sensing probe signifying the decrease in fluorescence signal, as shown in Figure 11a(e). Under UV irradiation, the fluorescence is increased, and the reduced modalities were visible to the naked eye, as seen in Figure 11b(a−e). Furthermore, Cys@Fe_3O_4Nps were also reused by treating Fe_3O_4 (Pb^{2+}-Cys-Ag^+) with an EDTA solution, as illustrated in Scheme 3.

2.6. Optimization of Bioassay Condition. To obtain better sensing performance of the proposed aptasensor, various experimental conditions were optimized, including the concentrations of $CaSnO_3$@PDANS, AO, and GC-rich ssDNA, and the effect of reaction time, pH, and temperature, by comparing the relative fluorescence changes.

The $CaSnO_3$@PDANS concentration utilized in this sensing system has a significant impact on the AO fluorescence quenching response. As a result, the fluorescence quenching efficacies of various $CaSnO_3$@PDANS concentrations were studied. As shown in Figure S5a, the fluorescence emission at 530 nm of 500 nM AO decreases as the amount of $CaSnO_3$@PDANS increases. However, when the concentration of $CaSnO_3$@PDANS was above 25 μg/mL, the AO emission remained unchanged. From the above results, a concentration of $CaSnO_3$@PDANS at 25 μg/mL was selected for the following analysis. Subsequently, the AO emission of the sensing system was improved by varying the concentration of GC-rich ssDNA, as the amount of highly stable G-quadruplex formed depends on the concentration of GC-rich ssDNA. The AO emission reached the maximum level due to the formation of the highly stable G-quadruplex with respective targets (Pb^{2+} and Ag^+). Therefore, the AO fluorescence emission ultimately depends on the concentration of GC-rich ssDNA. Accordingly, the concentration of GC-rich ssDNA was optimized within 50−700 nM, as shown in Figure S5b. The experimental results clearly show that the fluorescence intensity reached the utmost level when the concentration of GC-rich ssDNA was 500 nM. Further, the fluorescence intensity remains constant as a higher concentration of negatively charged DNA may result in steric hindrance or electrostatic repulsion. Therefore, the optimal

https://doi.org/10.1021/acsomega.1c04319
ACS Omega 2021, 6, 30580−30597

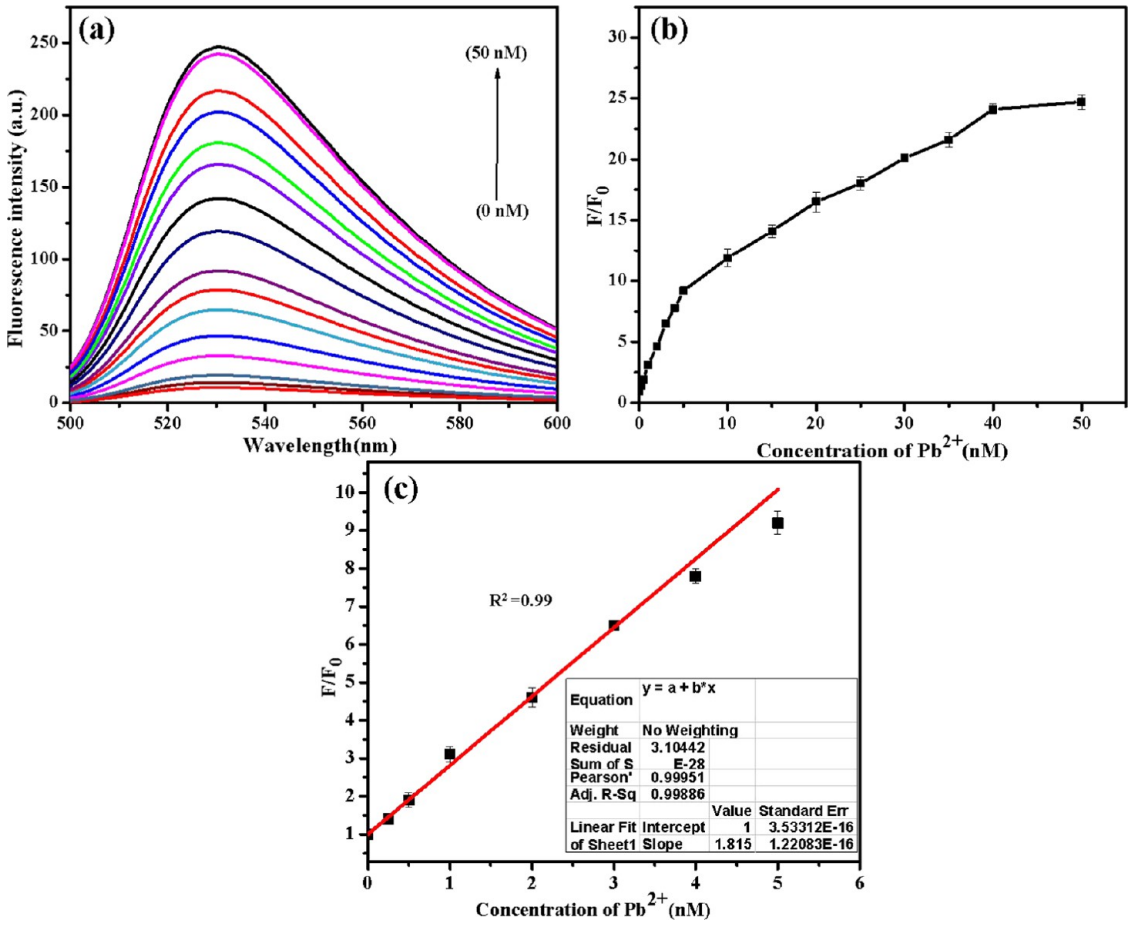

Figure 12. (a) Fluorescence emission spectra of the optimized aptasensor in the presence of different concentrations of Pb^{2+} (0, 0.25, 0.5,1, 2, 3, 4, 5, 10, 15, 20, 25, 30, 35, 40, and 50 nM). (b) Integrated fluorescence spectra against Pb^{2+} concentrations. (c) Linear plot of F/F_0 versus concentration of Pb^{2+} ions (0−5 nM); the inset shows the linear working equation.

concentration of GC-rich ssDNA (500 nM) was established as the fixed concentration for further studies.

Similarly, the fluorophore (AO) concentration was optimized from 50 to 700 nM (Figure S5c). The experimental results show that the AO fluorescence emission reached the maximum level at 500 nM of AO. Therefore, 500 nM AO was selected as the optimized concentration for this sensing system. The adsorption and desorption kinetics of AO on $CaSnO_3$@PDANS were studied by tracking changes in the AO emission over time. The kinetics of the fluorescence quenching reaction is quicker, and the emission of the fluorescence is reduced within 15 min. However, in the presence of target metal ions, the fluorescence gradually increased with incubation time, reaching a saturated fluorescence emission in 25 min. The experimental outcomes clearly show that the adsorbing and desorbing kinetics of AO on $CaSnO_3$@PDANS for 15 and 25 min were necessary for effective sensing processes, respectively (Figure S5d). Furthermore, the pH of the reaction is a crucial parameter for the accurate detection of targets. A pH value below 7 for the Pb^{2+} and Ag^{+} ions has reduced the affinity toward the guanine and cytosine bases due to the protonation of nitrogen atoms in the bases. When the pH is greater than 7, the fluorescence response is poor because of the partial participation of the hydroxide ions. Therefore, different pH values were optimized, as shown in Figure S5e. The fluorescence intensity values increased when the pH was 5−7.3. After increasing the pH of the solution to 7.3, the fluorescence intensity values slowly decreased. The performance of the sensing system was chosen for an optimized pH of 7.3. The influence of the reaction temperature on the performance of the sensing system was studied, and the optimized temperature was found to be 37 °C (Figure S5f).

2.7. Sensitivity and Selectivity Performance of the Pb^{2+} Aptasensor. The quantification was conducted on the basis of the optimal experimental conditions mentioned above. The relationship between the Pb^{2+}-ion concentration and fluorescence enhancement is shown in Figure 12. Figure 12a depicts the response of fluorescence spectra to a series of concentrations of Pb^{2+} ions. The intensity of the fluorescence increased significantly as the concentration of Pb^{2+} ions increased from 0 to 50 nM, which was consistent with an increased folding of the G-rich segment of the ssDNA into a G-quadruplex. This would reach saturation when the concentration of Pb^{2+} was above 50 nM (Figure 12b) and the fluorescence emission ratio showed a good linear relationship with the Pb^{2+} concentration between 0 and 5 nM as shown in Figure 12c. The detection limit for Pb^{2+} was 0.4 nM, which was achieved using the 3σ/slope method (where σ is the standard deviation of blank), which is significantly lower than the maximum allowable level of Pb^{2+} concentration in drinking water and food (U.S. Environmental Protection Agency EPA: 72 nM and International Agency for Research on Cancer IARC: 48.26 nM).[38] Therefore, our recyclable aptasensor detects Pb^{2+} quantitatively even at low concentrations, and can

https://doi.org/10.1021/acsomega.1c04319
ACS Omega 2021, 6, 30580−30597

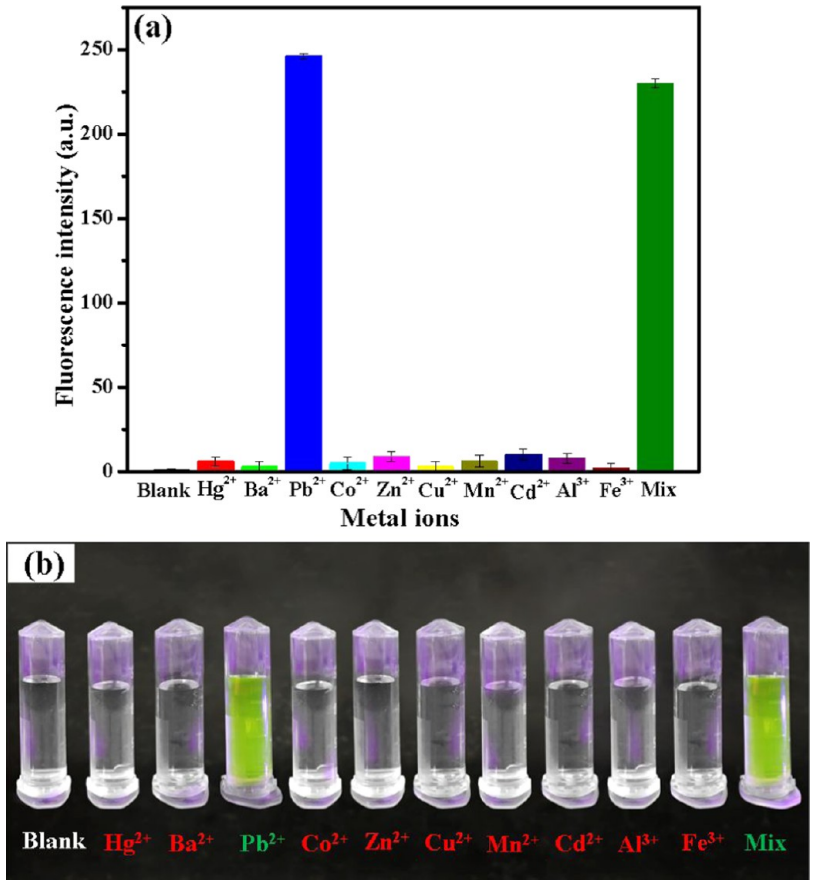

Figure 13. Selectivity of the Pb^{2+} sensor system. (a) Fluorescence response of the sensor in the presence of 50 nM Pb^{2+} ions and 100 nM of other metal ions. (b) Fluorescence dissimilarity toward Pb^{2+} ions and different metal ions by the naked eye under UV light.

be applied in real samples. As shown in Table S1, the suggested fluorometric aptasensor outperformed other previously reported sensors.

The selectivity of the proposed aptasensor is a very significant parameter for practical applications as several heavy metals are present in real water samples. Thus, the selectivity investigation of the developed Pb^{2+} sensor is very much mandatory. In this study, other metals, including Hg^{2+}, Zn^{2+}, Al^{3+}, Cu^{2+}, Fe^{3+}, Co^{2+}, Ba^{2+}, Mn^{2+}, Cd^{2+}, and the mixture of samples together with all of the metal ions (mix) were tested to evaluate the selectivity of the constructed fluorometric sensor. As shown in Figure 13a, the mentioned interference does not generate a response of the fluorometric sensor even at a much elevated concentration, but the Pb^{2+} ion exhibits a high fluorescence emission due to the formation of a stable G-quadruplex at a G-rich terminal of the ssDNA. Additionally, these fluorescence response processes can be seen with the naked eye under UV irradiation. The testing sample containing Pb^{2+} ions turned green in color, while the other solutions remained colorless (Figure 13b). The experimental result proves the excellent selectivity of the proposed biosensor, indicating its potential application in the analysis of complex samples.

2.8. Sensitivity and Selectivity Performance of the Ag^+ Aptasensor. Furthermore, the subsequent addition of the Ag^+ ion effectively enhances the fluorescence intensity, which clearly indicates the efficiency of our detection system toward Ag^+ too. Figure 14a describes the changes in the fluorescence intensity of AO upon incubation with Ag^+ ions. When the concentration of Ag^+ was increased from 0 to 25 nM, the fluorescence signal of AO was more intensified compared to the Pb^{2+} sensor, which was due to the increased stability of G-quadruplex. The formation of a duplex along with G-quadruplex at a C-rich segment of the DNA enabled the attainment of saturation when the concentration of Ag^+ was above 25 nM (Figure 14b). The signal response of Ag^+ concentration was linear in the range of 0−5 nM (Figure 14c), and the detection limit was 0.1 nM (according to the 3σ/slope method, where σ is the standard deviation of blank), which was significantly lower than the maximum allowable level of Ag^+ concentration in drinking water and food as defined by the U.S. Environmental Protection Agency, which is 10 nM.[3] Therefore, our recyclable aptasensor exhibits a quantitative detection limit that enables its suitability for the detection of Ag^+ even at low concentrations in real samples. Table S2 compares the linear ranges and detection limits of Ag^+ using various sensors. In contrast to the previously reported sensors, the LOD of our proposed method is quite low.

To verify the biosensing specificity toward the Ag^+ sensor, control experiments were performed by adding disruptors to the detecting samples. As shown in Figure 15a, metal-ion disruptors such as Co^{2+}, Al^{3+}, As^{5+}, Pb^{2+}, Fe^{3+}, Cu^{2+}, Hg^{2+}, K^+, and the mixture were added in the presence of Pb^{2+}-ion solution that does not significantly enhance the AO fluorescence emission. At the same time, there is an apparent enhancement of AO fluorescence from the Pb^{2+} sensor limit because of their high affinity between Ag^+ and C−C mismatch

https://doi.org/10.1021/acsomega.1c04319
ACS Omega 2021, 6, 30580−30597

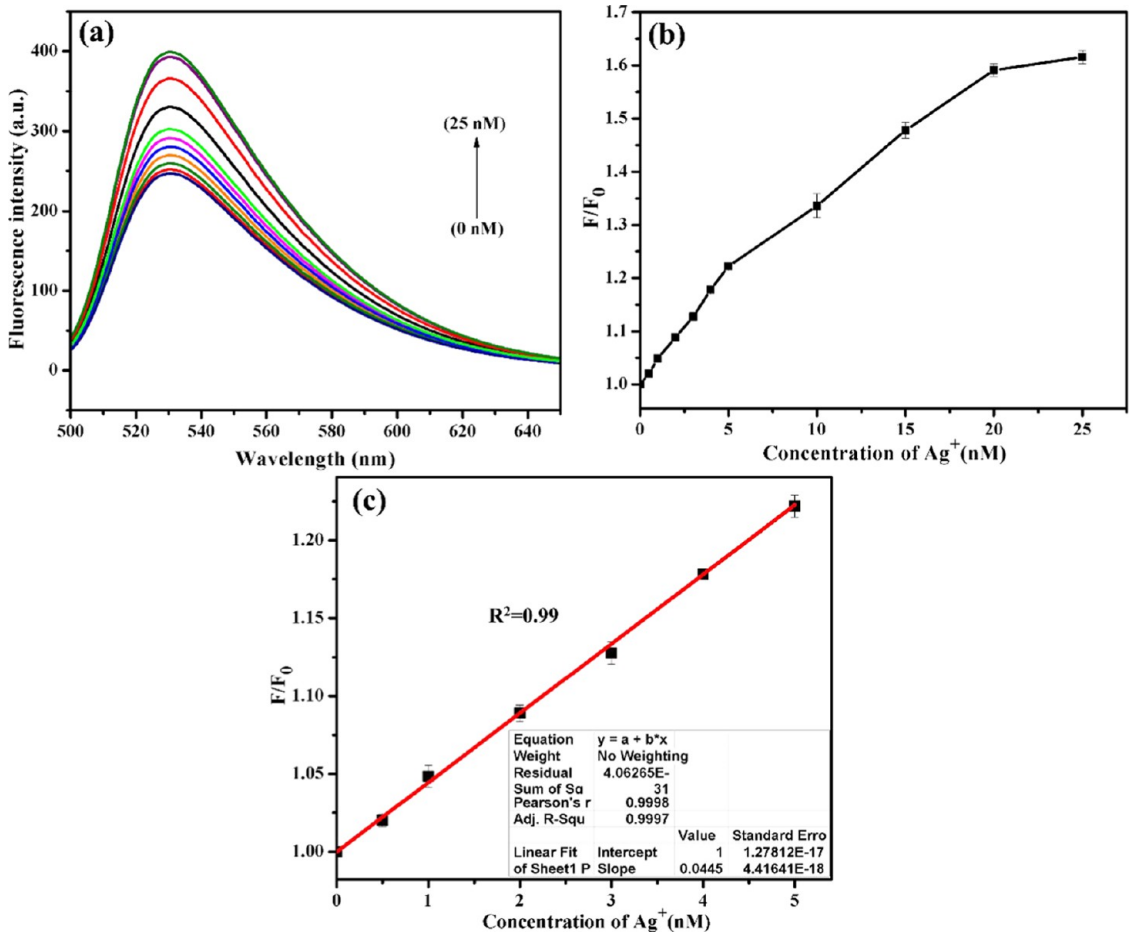

Figure 14. (a) Fluorescence emission spectra of the optimized aptasensor in the presence of different concentrations of Ag^+ (0, 0.5,1, 2, 3, 4, 5, 10, 15, 20, and 25 nM). (b) Integrated fluorescence spectra against Ag^+ concentrations. (c) Linear plot of F/F_0 versus concentration of Ag^+ ions (0−5 nM); the inset shows the linear working equation.

base pair in the 5′-terminal of G-quadruplex, resulting in the formation of a duplex structure. This demonstrates that the proposed sensor also had excellent selectivity for Ag^+ ions. Even though several other metal ions were present, these variations were easily detectable by the naked eye under UV irradiation. The sample containing Ag^+ ions turned into a dark greenish-yellow color, whereas the solution containing other metal ions did not reveal any color change, retaining the base green color as revealed in Figure 15b.

The proposed sensor selectivity for other organic compounds was also investigated, as shown in Figure 16a,b. It was discovered that none of the organic components triggered any interference, even at high concentrations. Furthermore, the detecting mechanism and the operating method of this sensor were much simpler than those mentioned in certain earlier reports on the detection of two or more metal ions (Table S3). Therefore, the above results clearly showed that the proposed sensor is established as the most selective nucleic acid-based sensor for Pb^{2+} and Ag^+.

2.9. Recyclability of the Aptasensor Probe. Reducing the detection cost through recycling of the sensing probe ($CaSnO_3$@PDANS/GC-rich ssDNA/AO) was considered pragmatic. It was important to observe that the majority of the existing Pb^{2+} and Ag^+ subsequent biosensors could not be recycled. The outlined research revealed the construction of a recyclable Pb^{2+} and Ag^+ biosensor using Cys@Fe_3O_4Nps. To recover its "original" detection probe $CaSnO_3$@PDANS/GC-rich ssDNA/AO, the pH and time of solution were optimized as shown in Figure 17a,b. The extent of the detection probe was recovered in appropriate amounts at pH of 7.3 and 7.4. It is important to note that the recovery experiments were conducted with an optimized pH of 7.4. The time needed for the recovery of the detection probe for the maximum extent was within 150 s. Thus, the release of the bound Pb^{2+} and Ag^+ ions was carried out at the buffer solution of a physiological pH 7.4 over 150 s.

Initially, in the sensing mechanism described in Scheme 2, the addition of Pb^{2+} into the $CaSnO_3$@PDANS/GC-rich ssDNA/AO probe resulted in the formation of the Pb^{2+}-stabilized G-quadruplex, leading to the recovery of AO emission. Next, the Ag^+ ion was induced into the $CaSnO_3$@PDANS/Pb^{2+}-AO-G-quadruplex, resulting in the formation of a duplex structure at the end of 5′-G-quadruplex, which highly stabilized the G-quadruplex structure, resulting in a maximum recovery of AO emission. After the first reaction with Pb^{2+} and Ag^+, Cys-Fe_3O_4Nps were added into the above solution, which strongly interacts with the target metal ions to form the Fe_3O_4 (Pb^{2+}−Cys−Ag^+) complex, which was confirmed by the EDX spectrum as shown in Figure S6. Further, an external magnetic field was applied to separate the Fe_3O_4 (Pb^{2+}−Cys−Ag^+) complex from the sensing system, resulting in the regeneration of the starting sensing probe. Hence, the recyclability of such biosensors for the subsequent recognition of Pb^{2+} and Ag^+ was assessed through consecutive reaction cycles. Figure 18

https://doi.org/10.1021/acsomega.1c04319
ACS Omega 2021, 6, 30580−30597

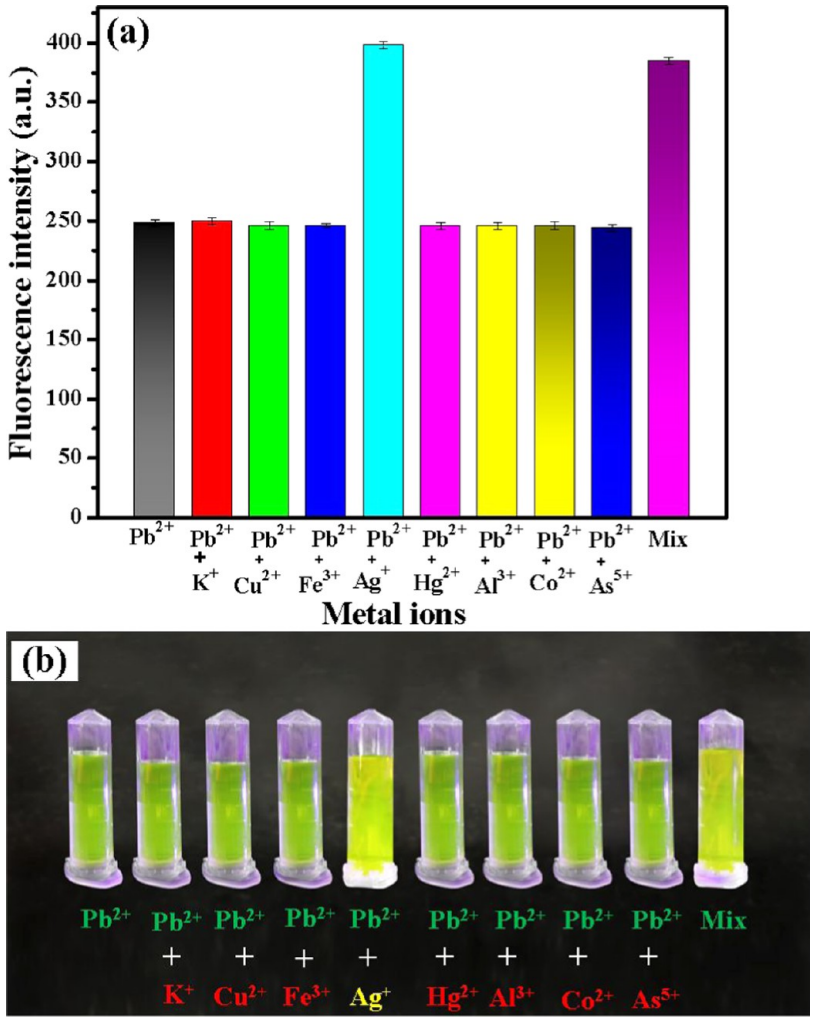

Figure 15. Selectivity of the Ag^+ sensor system. (a) Fluorescence response of the sensor in the presence of 25 nM Ag^+ and 100 nM of other metal ions with 50 nM Pb^{2+} ions. (b) Fluorescence dissimilarity toward Ag^+ and other metal ions with Pb^{2+} ions by the naked eye under UV light.

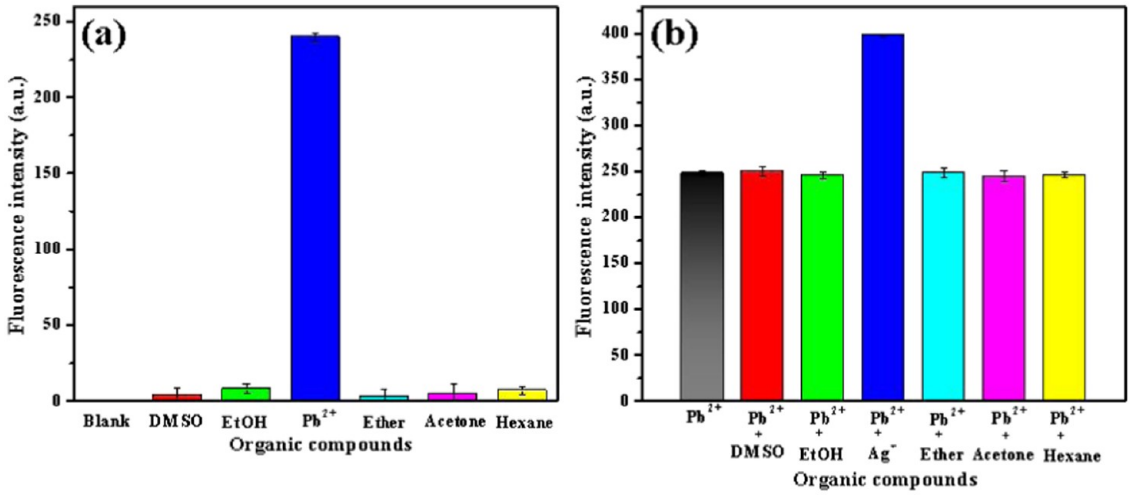

Figure 16. Selectivity of the sensor for Pb^{2+} (a) and Ag^+ (b) detection over other common organic compounds. The concentrations of Pb^{2+} and Ag^+ are 50 and 25 nM, respectively. The concentration of other organic compound is 1 μM.

describes the results of the cyclic detection of Pb^{2+} and Ag^+ ions. It was demonstrated that the proposed aptasensor could be used at least three times without any major changes in the fluorescence intensity, which established its recyclable nature. Moreover, almost 65% of the sensing probe was recovered via magnetic-driven separation after three consecutive cycles.

2.10. Reusability of Cys@Fe_3O_4Nps by EDTA. Ethylenediaminetetraacetic acid (EDTA) is a well-recognized metal

https://doi.org/10.1021/acsomega.1c04319
ACS Omega 2021, 6, 30580−30597

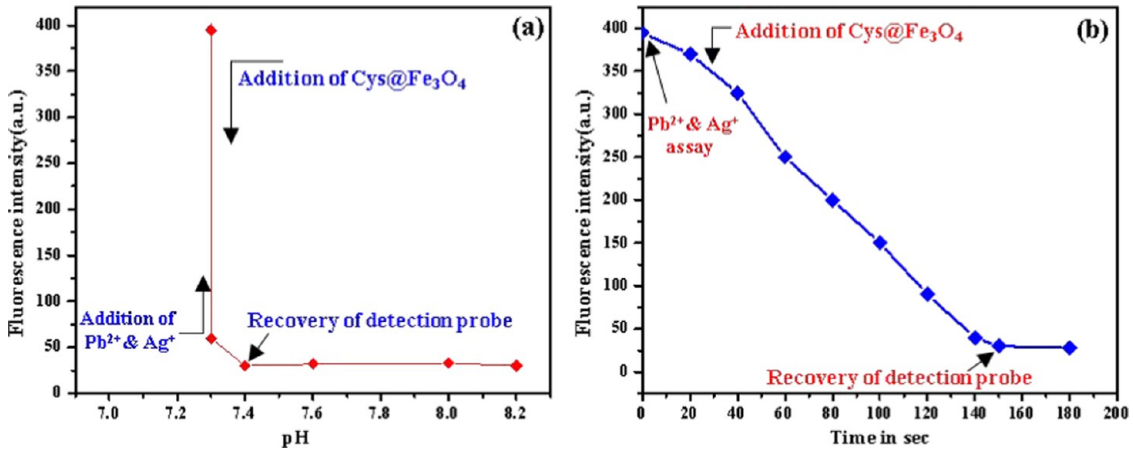

Figure 17. Effect of pH (a) and time (b) on the recovery of the detection probe.

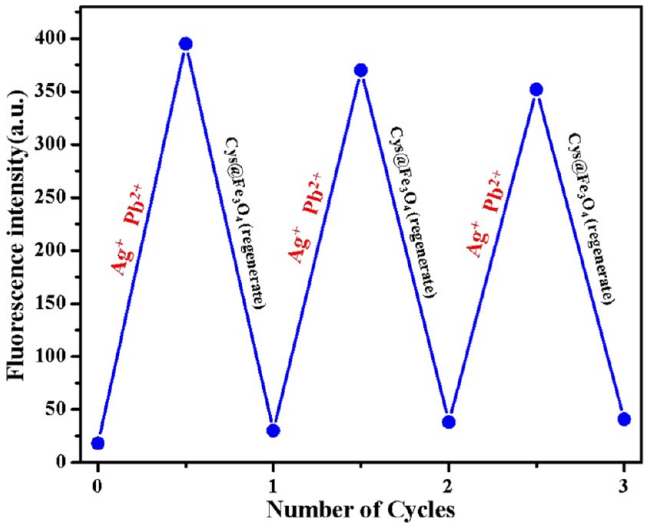

Figure 18. Efficiency of recyclable sensing probe for three times detection of targets.

chelator because of its extreme adsorbing capacity of metal cations. It provides six potential sites for bonding with metal ions, including four carboxyl and two amino groups.[39] Thus, desorption of Pb^{2+} and Ag^{+} ion capping was done on the surface of Cys@Fe_3O_4Nps using EDTA solution (0.1 mol/L). The Pb^{2+}- and Ag^{+}-ion-capped Cys@Fe_3O_4Nps were mixed with 10 mL of EDTA solution. After 1 h of treatment, the Pb^{2+} and Ag^{+} ions were desorbed from the Cys@Fe_3O_4Np surface and got dissolved in the EDTA solution. The solution was then filtered through a 0.2 μm membrane. The solid compound was carefully collected and washed numerous times with distilled water and dehydrated at 60 °C. In addition, the Pb^{2+}- and Ag^{+}-ion desorption from Cys@Fe_3O_4Nps was confirmed by EDX spectrum as shown in Figure S7.

2.11. Analytical Application. The applicability of our sensor was evaluated by targeting heavy metals in actual samples. The actual samples (lake water and tap water) were collected adjacent to the SRMIST campus in Tamil Nadu, India. The samples were centrifuged, and the supernatants were used for quantitative analysis. Some amount of Pb^{2+} and Ag^{+} was added to the lake water and tap water samples to simulate natural water with various concentrations (5, 10, and 15 nM) of Pb^{2+} and Ag^{+} ions. The reaction results are shown in Table 1, which reveals that the recovery of Pb^{2+} and Ag^{+} was between 95 and 102%, which indicated that the novel sensing probe system is remarkable for practical applications.

3. CONCLUSIONS

A novel recyclable fluorometric aptasensor ($CaSnO_3$@PDANS/GC-rich ssDNA/AO) was successfully developed to detect the Pb^{2+} and Ag^{+} ions by measuring the difference in AO emission (ΔAO_{em}) before and after the DNA interaction. The ΔAO_{em} values were monitored using photoluminescence spectroscopy, and naked eye observation was performed under UV irradiation. Sensitive detection of Pb^{2+} and Ag^{+} ions was achieved at levels as low as 0.4 and 0.1 nM, respectively, which are much lower than the EPA limits of Pb^{2+} (72 nM) and Ag^{+} (10 nM) in drinking water. Moreover, the Pb^{2+} and Ag^{+} probe exhibits high selectivity over other possible interference ions, fulfilling the requirements of several practical applications and excellent recyclability. Specifically, cysteine-modified magnetite nanoparticles (Cys@Fe_3O_4Nps) possess the ability to recycle the starting sensing probe, enabling the consecutive detection of targets. Furthermore, the Cys@Fe_3O_4Nps can also be reused after being treated with EDTA. Considering the facts

Table 1. Determination of Pb^{2+} and Ag^{+} Ions in Actual Samples Using Our Proposed Sensor[a]

samples	spiked (nM)	detected to Pb^{2+} ± SD	recovery (%)	detected to Ag^{+} ± SD	recovery (%)
lake water	5	$5.05^{x} \pm 1.12^{y}$	101.4	$5.02^{x} \pm 2.22^{y}$	101.4
	10	$10.26^{x} \pm 0.25^{y}$	101.3	$9.50^{x} \pm 1.89^{y}$	97.3
	15	$14.89^{x} \pm 1.3^{y}$	99.3	$15.5^{x} \pm 1.5^{y}$	99.3
tap water	5	$5.1^{x} \pm 1.12^{y}$	100.5	$5.50^{x} \pm 1.02^{y}$	101.4
	10	$9.89^{x} \pm 1.21^{y}$	98.95	$10.12^{x} \pm 0.99^{y}$	99.3
	15	$14.90^{x} \pm 1.2^{y}$	97.4	$14.50^{x} \pm 0.52^{y}$	96.3

[a] x, mean values of three determinations; y, standard deviation.

https://doi.org/10.1021/acsomega.1c04319
ACS Omega 2021, 6, 30580−30597

Scheme 4. Schematic Illustration of the Preparation of $CaSnO_3$ Microflower

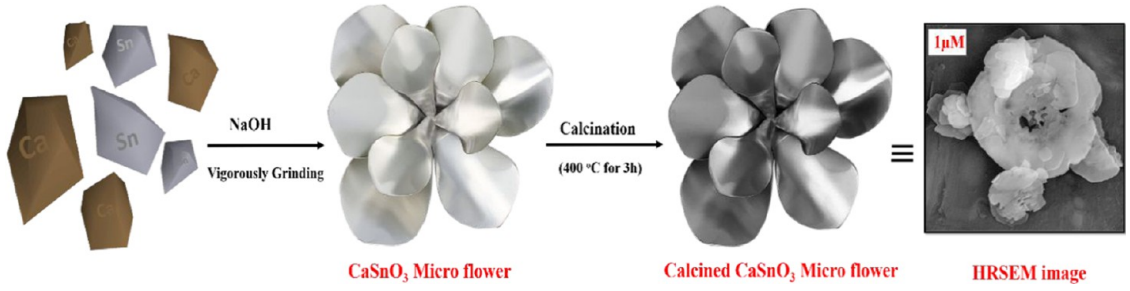

Scheme 5. Schematic Illustration of the Preparation of $CaSnO_3$@PDANS

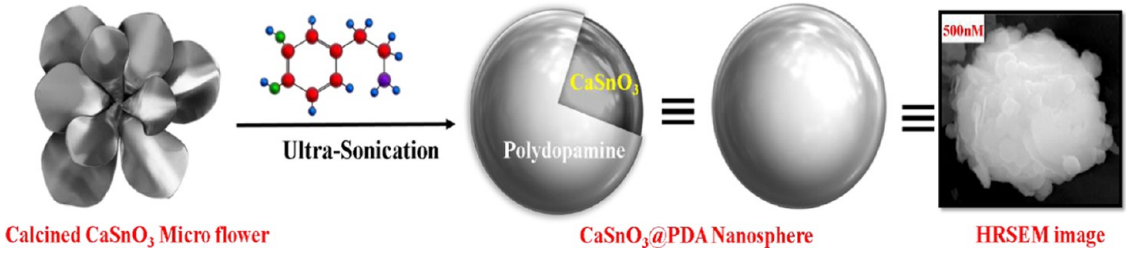

established, this aptasensor could be used as a realistic analytical tool for probing the Pb^{2+} and Ag^{+} ions due to its economical benefits. Hence, the design strategy of the mentioned aptasensor could definitely help in the development of a new fluorescence biosensor for the successful discrimination of other metal ions.

4. EXPERIMENTAL SECTION

4.1. Chemicals and Methods. Calcium nitrate, tin chloride, dopamine, acridine orange, L-cysteine, EDTA, and tris hydrochloride buffer salt were obtained from Sigma-Aldrich. The sensing-related DNA samples were procured from Integrated DNA Technologies, and the DNA sequences used in this paper are listed as follows.

DNA1: 3′-CTGGAAGGAAAGGAAGGCCTACTTCGAC-TACAGTCTCAG-5′

DNA2: 3′-TACGGATCGATGATCGGATCATCG-CAGTCC-5′

DNA3: 3′-TAGGGTTGGGTATGGGAAGGGTCCCTC-CAACCTATACCTTCCACCCA-5′

DNA4: 3′-TTAGGATCTGGTTACTCCGTCTACCT-5′

DNA5: 3′-TCGACGTAGCTATCGTACGCCTACCTC-TA-5′

The stock solution of aptamer was prepared by dissolving 50 mM Tris-HCl buffer and stored at 4 °C. The nitrate salts of lead, silver, mercury, calcium, and nickel, and the chloride salts of cobalt, copper, barium, ferric, magnesium, ferrous, manganese, and other standard chemicals were purchased at the highest purity levels from SRL and Sigma-Aldrich (India). Throughout the experiment, deionized (DI) water was used.

4.2. Structural Characterization. The excitation and emission intensities of the sensor were recorded by a spectrofluorometer (HORIBA JOBIN YVON Fluoromax-4), and light from a standard xenon lamp is used as the excitation source. Absorption measurements were performed using a UV−vis absorption spectrophotometer (Shimadzu, UV-2600). The morphological appearances of the CaSnO3@PDANS were obtained using a high-resolution scanning electron microscope (HRSEM, Nanosem 430), and the inner morphologies of the synthesized nanoparticles were identified using a high-resolution transmission electron microscope (HR-TEM, JEOL/JEM 2100). Energy-dispersive X-ray spectroscopy (EDXS) of ISIS300 was used to recognize the distribution of Ca^{2+} and Sn^{4+} ions, carbon, nitrogen, and oxygen profiles on the surface of the $CaSnO_3$ and the $CaSnO_3$@PDA. A Fourier transform infrared (FT-IR) spectrometer was used to detect the presence of functional groups (Agilent Resolution Pro). X-ray diffraction (XRD) measurements utilizing a PAN analytical X'Pert powder diffractometer with Cu-K radiations were used to determine the crystalline and amorphous nature of the samples. The surface element composition and charge of CaSnO3@PDANS were estimated using an X-ray photoelectron spectrometer (XPS, PerkinElmer Phi 1600 ESCA system) with magnesium as the radiation source. A digital pH meter (PHS-3C) was used to optimize the pH of the sensing system.

4.3. Preparation of $CaSnO_3$ Microflower. The $CaSnO_3$ microflower was synthesized using a simple two-step solid-state reaction method, as reported earlier with some major modifications.[40] In a typical process, 3 g of solid calcium nitrate and 3 g of tin chloride were separately ground to a fine powder using a mortar and pestle. The finely ground powder was combined with 2 g of preweighed sodium hydroxide followed by rapid grinding of the mixture for 60 min. During the grinding process, white smoke comes out and an enormous amount of heat is released. The final product was rinsed multiple times using DI water and dehydrated at 70 °C for 5 h. The resulting material was further calcined at 400 °C for 3 h to obtain the final $CaSnO_3$ microflower, as illustrated in Scheme 4.

4.4. Preparation of $CaSnO_3$@PDA Nanosphere. $CaSnO_3$@PDANS synthesis was completed at room temperature employing a simple and uncomplicated ultrasonication method. In brief, 500 mg of polydopamine was ultrasonically treated with 500 mg of $CaSnO_3$ in 50 mL of DI H_2O for 45 min. The resulting suspensions were properly filtered and rinsed many times with DI H_2O and C_2H_5OH before being dried in an oven overnight at 70 °C (Scheme 5).

https://doi.org/10.1021/acsomega.1c04319
ACS Omega 2021, 6, 30580−30597

Scheme 6. Schematic Representation of the Synthesis of Cys@Fe_3O_4Nps

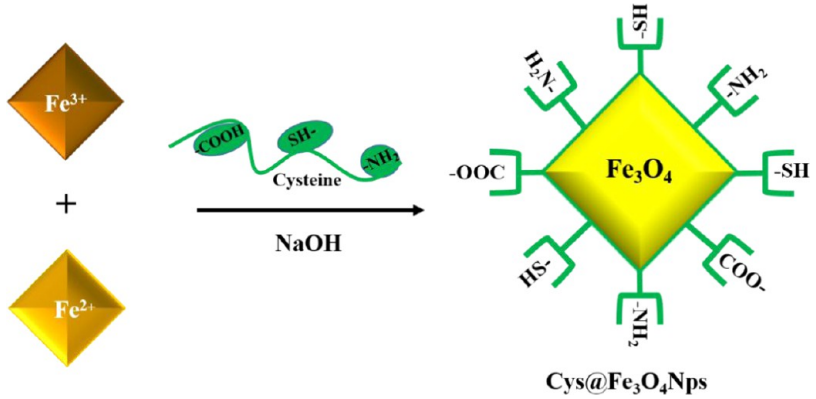

4.5. Preparation of Recyclic Probe. Cysteine-functionalized magnetite nanoparticles (Cys@Fe_3O_4Nps) were synthesized using the coprecipitation method discussed previously with additional modifications.[41] L-Cys (0.1 g) was dissolved in 20 mL of H_2O with pH 4.0−6.0. Then, 2.0 g of ferric chloride and 1.0 g of ferrous chloride were dissolved in 50 mL of H_2O and heated to 80 °C. Simultaneously, 10 mL of sodium hydroxide solution and the prepared 20 mL of L-Cys solution were added to the preceding solution. The mixture was heated further for 45 min at 80 °C before being cooled to normal temperature. The final dark precipitate was washed many times with water to separate the pure nanoparticles. After this, the pure Cys@Fe_3O_4Nps (black precipitate) were dried at 70 °C for 5 h (Scheme 6). Finally, the desired recycle probe was achieved and then characterized using FT-IR, XRD, HRSEM, and EDXS, as shown in Figures S1−S4, respectively.

4.6. Procedure for Pb^{2+} and Ag^+ Detection. A typical analysis method for the recognition of Pb^{2+} and Ag^+ is given as follows. Initially, 500 μL of 500 nM AO and GC-rich ssDNA were both prepared using Tris HCl buffer and mixed together. This is followed by the addition of 25 μg/mL $CaSnO_3$@PDANS into the microcentrifuge tube. After 15 min, the solution was transferred into a cuvette and the fluorescence spectra were measured at the excitation and emission wavelengths of 490 and 530 nm, respectively. The spectra revealed a drop in AO fluorescence due to the quenching performance of $CaSnO_3$@PDANS. Following this, a freshly prepared desired concentration of Pb^{2+} solution was added to the overhead solution and incubated for 15 min at 37 °C, resulting in the formation of G-quadruplex and an increase in the fluorescence emission of AO, which is directly proportional to the Pb^{2+} concentration. Next, a desired amount of Ag^+ is added and incubated for 10 min at 37 °C, resulting in the formation of a duplex structure along with a G-quadruplex structure, which results in a further increase of fluorescence equal to the quantity of the Ag^+ ions. Similarly, the proposed sensing probe was regenerated by the elimination of Pb^{2+} and Ag^+ using Cys@Fe_3O_4Nps, resulting in the turn-off of the fluorescence signal.

■ ASSOCIATED CONTENT

Supporting Information

The Supporting Information is available free of charge at https://pubs.acs.org/doi/10.1021/acsomega.1c04319.

Detailed characterization and explanation of recycling probe Cys@Fe_3O_4 (Figures S1−S4), optimization of aptasensor conditions (Figure S5), EDXS confirmation of sensing probe and Cys@Fe_3O_4 recyclability (Figures S6 and S7), and comparison of the sensing performance of this method with the previously reported methods for the detection of Pb^{2+} and Ag^+ (Tables S1−S3) (PDF)

■ AUTHOR INFORMATION

Corresponding Author

Panneerselvam Perumal − *Department of Chemistry, SRM Institute of Science and Technology, Kattankulathur 603203 Tamil Nadu, India;* orcid.org/0000-0003-2647-6835; Phone: +91 9688538842; Email: panneerp1@srmist.edu.in, panneerchem82@gmail.com

Authors

Arunjegan Amalraj − *Department of Chemistry, SRM Institute of Science and Technology, Kattankulathur 603203 Tamil Nadu, India*

Rajaji Pavadai − *Department of Chemistry, SRM Institute of Science and Technology, Kattankulathur 603203 Tamil Nadu, India*

Complete contact information is available at: https://pubs.acs.org/10.1021/acsomega.1c04319

Notes

The authors declare no competing financial interest.

■ ACKNOWLEDGMENTS

The authors acknowledge the Department of Chemistry, SRM Institute of Science and Technology, Tamil Nadu - 603 203, India, for providing the necessary facilities to complete the research work.

■ REFERENCES

(1) Radhakrishnan, K.; Sivanesan, S.; Panneerselvam, P. Turn-On Fluorescence Sensor Based Detection of Heavy Metal Ion Using Carbon Dots@graphitic-Carbon Nitride Nanocomposite Probe. *J. Photochem. Photobiol., A* **2020**, *389*, No. 112204.

(2) Tchounwou, P. B.; Yedjou, C. G.; Patlolla, A. K.; Sutton, D. J. Heavy Metal Toxicity and the Environment. In *Molecular, Clinical and Environmental Toxicology*; 2012; Vol. 3, pp 133−164.

(3) Lin, Z.; Li, X.; Kraatz, H. B. Impedimetric immobilized DNA-based sensor for simultaneous detection of Pb^{2+}, Ag^+, and Hg^{2+}. *Anal. Chem.* **2011**, *83*, 6896−901.

(4) Zhu, G.; Zhang, C. Y. Functional Nucleic Acid-Based Sensors for Heavy Metal Ion Assays. *Analyst* **2014**, *139*, 6326−6342.

(5) Yang, C.; Yang, S.; Li, J.; Du, Y.; Song, L.; Huang, D.; Chen, J.; Zhou, Q.; Yang, Q.; Tang, Y. Intelligent Sensors of Lead Based on a Reconfigurable DNA-Supramolecule Logic Platform. *Anal. Chem.* **2018**, *90*, 10585−10590.
(6) Rajaji, P.; Panneerselvam, P. A Novel Polydopamine Grafted 3D MOF Nanocubes Mediated GR-5/GC DNAzyme Complex with Enhanced Fluorescence Emission Response toward Spontaneous Detection of Pb(II) and Ag(I) Ions. *ACS Omega* **2020**, *5*, 25188−25198.
(7) Gorkhali, R.; Huang, K.; Kirberger, M.; Yang, J. J. Defining Potential Roles of Pb2+ in Neurotoxicity from a Calciomics Approach. *Metallomics* **2016**, *8*, 563−578.
(8) Ishida, T. Antibacterial Mechanism of Ag+ Ions for Bacteriolyses of Bacterial Cell Walls via Peptidoglycan Autolysins, and DNA Damages. *MOJ Toxicol.* **2018**, *4*, 345−350.
(9) Liu, G.; Yuan, Y.; Wei, S.; Zhang, D. Impedimetric DNA-Based Biosensor for Silver Ions Detection with Hemin/G-Quadruplex Nanowire as Enhancer. *Electroanalysis* **2014**, *26*, 2732−2738.
(10) Saito, S.; Danzaka, N.; Hoshi, S. Direct Fluorescence Detection of Pb^{2+} and Cd^{2+} by High-Performance Liquid Chromatography Using 1-(4-Aminobenzyl)Ethylenediamine-N, N,N′,N′-Tetraacetate as a Pre-Column Derivatizing Agent. *J. Chromatogr. A* **2006**, *1104*, 140−144.
(11) Ghorbani, M.; Akbarzade, S.; Aghamohammadhasan, M.; Seyedin, O.; Afshar Lahoori, N. Pre-Concentration and Determination of Cadmium and Lead Ions in Real Water, Soil and Food Samples Using a Simple and Sensitive Green Solvent-Based Ultrasonic Assisted Dispersive Liquid-Liquid Microextraction and Graphite Furnace Atomic Absorption Spectrom. *Anal. Methods* **2018**, *10*, 2041−2047.
(12) Zhao, L.; Zhong, S.; Fang, K.; Qian, Z.; Chen, J. Determination of Cadmium(II), Cobalt(II), Nickel(II), Lead(II), Zinc(II), and Copper(II) in Water Samples Using Dual-Cloud Point Extraction and Inductively Coupled Plasma Emission Spectrometry. *J. Hazard. Mater.* **2012**, *239*−*240*, 206−212.
(13) Ganjali, M. R.; Daftari, A.; Hajiagha-Babaei, L.; Badiei, A.; Saberyan, K.; Ziarani, G. M.; Moghimi, A. Pico Level Monitoring of Silver with Modified Hexagonal Mesoporous Compound (MCM-41) and Inductively Coupled Plasma Atomic Emission Spectrometry. *Water. Air. Soil Pollut.* **2006**, *173*, 71−80.
(14) Ghaedi, M.; Shokrollahi, A.; Niknam, K.; Niknam, E.; Najibi, A.; Soylak, M. Cloud Point Extraction and Flame Atomic Absorption Spectrometric Determination of Cadmium(II), Lead(II), Palladium-(II) and Silver(I) in Environmental Samples. *J. Hazard. Mater.* **2009**, *168*, 1022−1027.
(15) Shamspur, T.; Mashhadizadeh, M. H.; Sheikhshoaic, I. Flame Atomic Absorption Spectrometric Determination of Silver Ion after Preconcentration on Octadecyl Silica Membrane Disk Modified with Bis[5-((4-Nitrophenyl)Azosalicylaldehyde)] as a New Schiff Base Ligand. *J. Anal. At. Spectrom.* **2003**, *18*, 1407−1410.
(16) Kassem, M. A. Development of a Cloud-Point Extraction Method for Spectrophotometric Nano Determination of Silver in Real Samples. *Anal. Methods* **2015**, *7*, 6747−6754.
(17) Arunjegan, A.; Rajaji, P.; Sivanesan, S.; Panneerselvam, P. A Turn-ON Fluorometric Biosensor Based on SsDNA Immobilized with a Metal Phenolic Nanomaterial for the Sequential Detection of Pb(II) and Epirubicin Cancer Drug. *RSC Adv.* **2021**, *11*, 12361−12373.
(18) Xi, H.; Cui, M.; Li, W.; Chen, Z. Colorimetric Detection of Ag^{+} Based on C−Ag^{+}−C Binding as a Bridge between Gold Nanoparticles. *Sens. Actuators, B* **2017**, *250*, 641−646.
(19) Li, T.; Wang, E.; Dong, S. Lead(II)-Induced Allosteric G-Quadruplex DNAzyme as a Colorimetric and Chemiluminescence Sensor for Highly Sensitive and Selective Pb2+ Detection. *Anal. Chem.* **2010**, *82*, 1515−1520.
(20) Ding, Y.; Wang, S.; Li, J.; Chen, L. Nanomaterial-based optical sensors for mercury ions. *TrAC Trends in Analytical Chemistry* **2016**, *82*, 175−190.
(21) Lou, T.; Chen, Z.; Wang, Y.; Chen, L. Blue-to-red colorimetric sensing strategy for Hg2+ and Ag+ via redox-regulated surface chemistry of gold nanoparticles. *ACS Appl. Mater. Interfaces* **2011**, *3*, 1568−1573.
(22) Muppidathi, M.; Perumal, P.; Ayyanu, R.; Subramanian, S. Immobilization of ssDNA on a metal−organic framework derived magnetic porous carbon (MPC) composite as a fluorescent sensing platform for the detection of arsenate ions. *Analyst.* **2019**, *144*, 3111−3118.
(23) Radhakrishnan, K.; Kumar, P. S. Target-receptive structural switching of ssDNA as selective and sensitive biosensor for subsequent detection of toxic Pb^{2+} and organophosphorus pesticide. *Chemosphere* **2021**, *287*, No. 132163.
(24) Shi, X.; Gu, W.; Peng, W.; Li, B.; Chen, N.; Zhao, K.; Xian, Y. Sensitive Pb^{2+} Probe Based on the Fluorescence Quenching by Graphene Oxide and Enhancement of the Leaching of Gold Nanoparticles. *ACS Appl. Mater. Interfaces* **2014**, *6*, 2568−2575.
(25) Venkateswarlu, S.; Reddy, A. S.; Panda, A.; Sarkar, D.; Son, Y.; Yoon, M. Reversible Fluorescence Switching of Metal-Organic Framework Nanoparticles for Use as Security Ink and Detection of Pb^{2+} Ions in Aqueous Media. *ACS Appl. Nano Mater* **2020**, *3*, 3684−3692.
(26) Liu, Y. M.; Ju, X. J.; Xin, Y.; Zheng, W. C.; Wang, W.; Wei, J.; Xie, R.; Liu, Z.; Chu, L. Y. A Novel Smart Microsphere with Magnetic Core and Ion-Recognizable Shell for Pb^{2+} Adsorption and Separation. *ACS Appl. Mater. Interfaces* **2014**, *6*, 9530−9542.
(27) Ravikumar, A.; Panneerselvam, P.; Radhakrishnan, K.; Christus, A. A. B.; Sivanesan, S. MoS 2 Nanosheets as an Effective Fluorescent Quencher for Successive Detection of Arsenic Ions in Aqueous System. *Appl. Surf. Sci.* **2018**, *449*, 31−38.
(28) Chen, L.; Fu, X.; Lu, W.; Chen, L. Highly sensitive and selective colorimetric sensing of Hg2+ based on the morphology transition of silver nanoprisms. *ACS Appl. Mater. Interfaces* **2013**, *5*, 284−290.
(29) Fu, X.; Lou, T.; Chen, Z.; Lin, M.; Feng, W.; Chen, L. "Turn-on" fluorescence detection of lead ions based on accelerated leaching of gold nanoparticles on the surface of graphene. *ACS Appl. Mater. Interfaces* **2012**, *4*, 1080−1086.
(30) Jiang, X.; Xu, W.; Chen, X.; Liang, Y. Colorimetric assay for ultrasensitive detection of Ag (I) ions based on the formation of gold nanoparticle oligomers. *Anal. Bioanal. Chem.* **2019**, *11*, 2439−2445.
(31) Poinard, B.; Neo, S. Z. Y.; Yeo, E. L. L.; Heng, H. P. S.; Neoh, K. G.; Kah, J. C. Y. Polydopamine Nanoparticles Enhance Drug Release for Combined Photodynamic and Photothermal Therapy. *ACS Appl. Mater. Interfaces* **2018**, *10*, 21125−21136.
(32) Chen, F.; Xing, Y.; Wang, Z.; Zheng, X.; Zhang, J.; Cai, K. Nanoscale Polydopamine (PDA) Meets π-π Interactions: An Interface-Directed Coassembly Approach for Mesoporous Nanoparticles. *Langmuir* **2016**, *32*, 12119−12128.
(33) Muthukutty, B.; Krishnapandi, A.; Chen, S. M.; Abinaya, M.; Elangovan, A. Innovation of Novel Stone-Like Perovskite Structured Calcium Stannate ($CaSnO_3$): Synthesis, Characterization, and Application Headed for Sensing Photographic Developing Agent Metol. *ACS Sustainable Chem. Eng.* **2020**, *8*, 4419−4430.
(34) Cheng, W.; Fan, F.; Zhang, Y.; Pei, Z.; Wang, W.; Pei, Y. A Facile Approach for Fabrication of Core-Shell Magnetic Molecularly Imprinted Nanospheres towards Hypericin. *Polymers* **2017**, *9*, No. 135.
(35) Tsega, M.; Dejene, F. B. Synthesis and Luminescence in Sol − Gel Auto-Combustion-Synthesized $CaSnO_3$: Eu^{3+} Phosphor. *Bull. Mater. Sci.* **2017**, *40*, 1347−1354.
(36) Sudhaparimala, S.; Gnanamani, A.; Mandal, A. B. Egg Shell Powder as the Precursor for the Synthesis of Nano Crystalline Calcium Stannate ($CaSnO_3$) with orthorhombic Perovskite Structure: Exploration on Phase, Morphology and Antioxidant Property. *Chem. Sci. Rev. Lett.* **2012**, *2*, 267−277.
(37) Xi, J.; Xiao, J.; Xiao, F.; Jin, Y.; Dong, Y.; Jing, F.; Wang, S. Mussel-Inspired Functionalization of Cotton for Nano-Catalyst

https://doi.org/10.1021/acsomega.1c04319
ACS Omega 2021, 6, 30580−30597

Support and Its Application in a Fixed-Bed System with High Performance. *Sci. Rep.* **2016**, *6*, No. 21904.
(38) Wang, L.; Wen, Y.; Li, L.; Yang, X.; Jia, N.; Li, W.; Meng, J.; Duan, M.; Sun, X.; Liu, G. Sensitive and label-free electrochemical lead ion biosensor based on a DNAzyme triggered G-quadruplex/hemin conformation. *Biosensors and Bioelectronics* **2018**, *115*, 91−96.
(39) Jiang, Y.; Liu, C.; Huang, A. EDTA-Functionalized Covalent Organic Framework for the Removal of Heavy-Metal Ions. *ACS Appl. Mater. Interfaces* **2019**, *11*, 32186−32191.
(40) Zhang, X.; Hu, J.; Cao, Y.; Xie, J.; Jia, W.; Wang, S.; Jia, D. Insights into Crystal Facets of Perovskite SrSnO3 as High-Performance Photocatalysts toward Environmental Remediation. *Chem. - Eur. J.* **2018**, *24*, 14111−14118.
(41) Bagbi, Y.; Sarswat, A.; Mohan, D.; Pandey, A.; Solanki, P. R. Lead and Chromium Adsorption from Water Using L-Cysteine Functionalized Magnetite (Fe_3O_4) Nanoparticles. *Sci. Rep.* **2017**, *7*, No. 7672.

https://doi.org/10.1021/acsomega.1c04319
ACS Omega 2021, 6, 30580−30597